JGR Solid Earth

RESEARCH ARTICLE
10.1029/2021JB022569

The Spatial Relationship Between Contemporaneous Tremor Detections in Relatively Low- and High-Frequency Bands

Chao Song[1] **and Allan M. Rubin**[1]

[1]Department of Geosciences, Princeton University, Princeton, NJ, USA

Key Points:

- Coherent tremor signals are detected and located separately in relatively high-frequency (1.25–6.5 Hz) and low-frequency (0.5–1.25 Hz) bands
- LF signals seem to consistently lag contemporaneous HF signals by ~500 m relative to the propagating fronts of rapid tremor migrations
- Persistent offsets suggest that LF signals may have a source distinct from just the temporal overlapping of typical higher-frequency LFEs

Supporting Information:

Supporting Information may be found in the online version of this article.

Correspondence to:

C. Song,
chaosong@princeton.edu

Citation:

Song, C., & Rubin, A. M. (2021). The spatial relationship between contemporaneous tremor detections in relatively low- and high-frequency bands. *Journal of Geophysical Research: Solid Earth*, *126*, e2021JB022569. https://doi.org/10.1029/2021JB022569

Received 8 JUN 2021
Accepted 31 OCT 2021

Abstract Although tremor is believed to consist of myriad low-frequency earthquakes (LFEs), it also contains longer-period signals of unknown origin. We investigate the source of some of the longer-period signals by locating tremor windows independently in relatively high-frequency ("HF", 1.25–6.5 Hz, containing typical LFEs) and low-frequency ("LF", 0.5–1.25 Hz) bands. We hypothesize that if tremor consists entirely of LFEs, such that the lower-frequency signals come from the non-uniform timing of higher-frequency (~2 Hz) LFEs, then contemporaneous LF and HF signals should be nearly co-located. Here we search for a systematic offset between the locations of contemporaneous LF and HF detections during rapid tremor migrations (RTMs). This first requires correcting for apparent offsets in location that arise simply from filtering in different passbands. To guard against possible errors in our empirical filtering effect corrections, we focus on a region of the subduction interface beneath southern Vancouver Island that hosts migrations propagating in nearly opposing directions. We find that the LF energy appears to occur roughly 500 m farther behind the propagating fronts of RTMs than the HF energy, whether those fronts propagate to the ENE or to the WSW. This separation is small compared to the location error of individual LF detections, but the result seems robust owing to the large number of detections. If this result stands, it suggests that tremor consists of more than just a collection of LFEs, with longer-period energy being generated farther behind the migrating fronts of RTMs, where slip speeds are presumably lower.

Plain Language Summary Tectonic tremor is a poorly-understood seismic signal emanating from great depth along plate-bounding faults. It typically occurs in bursts of activity that correspond to "rapid tremor migrations". Tremor contains myriad, sometimes impulsive arrivals termed low-frequency earthquakes (LFEs), but it also contains longer-period signals whose origin is debated. Investigating these longer-duration signals is hampered by their generally low signal-to-noise ratio, mostly due to the presence of the Earth's microseismic noise band from ~0.1–1 Hz. We find that beneath southern Vancouver Island the signal-to-noise ratio is often high enough to locate tremor in both the typical frequency band used for tremor and LFEs (≳2 Hz) and within the upper end of the microseismic band (down to 0.5 Hz). In this study we show that the lower-frequency signals appear to locate farther behind the propagating fronts of rapid tremor migrations, by about 500 m, than the higher-frequency signals containing typical LFEs. This spatial offset suggests that the longer-period signal in tremor does not arise simply from the clustering in time and space of more familiar higher-frequency LFEs. It also suggests that the same portion of the fault might produce energy of different frequencies at different times, depending upon the loading conditions.

1. Introduction

Nonvolcanic tremor, also known as tectonic tremor, was first detected occurring deep within subduction zones, at depths of ~35–45 km along the subduction interface (Obara, 2002). Tremor is a low-amplitude, extended-duration signal often lacking clear impulsive arrivals, and is dominated by frequencies from 1–10 Hz (Beroza & Ide, 2011). Tremor is associated in space and time with geodetically-observed slow slip events (e.g., Bartlow et al., 2011; Frank et al., 2014; Ito et al., 2007; Rousset et al., 2019). On the time scale of episodic tremor and slip (ETS) episodes, tremor in multiple subduction zones migrates along strike at speeds of 5–15 km/d over a period of weeks (e.g., Armbruster et al., 2014; Ghosh et al., 2009; Ito et al., 2007; Kao et al., 2009; Obara, 2002, 2010; Wech & Creager, 2008). On shorter time scales, rapid tremor reversals (RTRs) propagate several tens of kilometers back along strike over many hours (Houston et al., 2011), at

speeds several tens of times faster than the main front. On even shorter time scales, rapid tremor migrations (RTMs) propagate 5–20 km over periods of several minutes to a couple of hours (e.g., Bostock et al., 2015; Ghosh et al., 2010; Obara et al., 2012; Peng et al., 2015; Rubin & Armbruster, 2013), at speeds up to hundreds of times faster than the main front. Both faster migration styles usually start near the main tremor front and propagate either back along strike (RTRs and some RTMs), or along the main front (other RTMs), although in some regions, perhaps where tremor is more sparse, RTMs appear to initiate at greater distances behind a poorly-defined front (Peng & Rubin, 2017; Shelly et al., 2007a).

Often embedded within tremor are low-frequency earthquakes (LFEs), characterized by low dominant frequencies compared to regular earthquakes of similar magnitude, typically 1–2 (Katsumata & Kamaya, 2003). LFEs are sometimes impulsive enough to stand out above contemporaneous tremor (Katsumata & Kamaya, 2003); at other times or in other places they have been identified only by auto-correlation of seismograms across an entire seismic network (Brown et al., 2008; Bostock et al., 2012; Shelly, 2010). Varying slightly with tectonic setting, the dominant frequency band for detecting LFEs is generally similar to that of the contemporaneous tremor (e.g., Bostock et al., 2015; Chestler & Creager, 2017; Ide, Shelly, & Beroza, 2007; Thomas et al., 2016). There are exceptions to the typical frequency range of ∼1–10 Hz; detection of both tremor and LFEs beneath Guerrero, Mexico, have been more successful in the 1–2 Hz passband, presumably because of a much narrower range of good signal-to-noise ratio (Frank et al., 2014; Peng & Rubin, 2017). Since the pioneering work of Shelly et al. (2006, 2007b), it has become well-accepted that tremor consists in large part of a swarm of LFEs, whose focal mechanisms are consistent with shear slip on the slab interface in the direction of plate motion (Brown et al., 2009; Ide, Shelly, & Beroza, 2007; Shelly et al., 2006; Wech & Creager, 2007). However, whether tremor consists entirely of LFEs, or includes longer-period sources distinct from LFEs, remains debated.

Regional studies show that LFEs tend to have a characteristic duration. Using in each case a 2–8 Hz passband, durations were found to be about 0.3 s in west Japan (Ide, Shelly, & Beroza, 2007), about 0.2 s in Parkfield (Thomas et al., 2016), and 0.25–0.4 s in Cascadia (Chestler & Creager, 2017). Bostock et al. (2012) used a somewhat wider passband of 1–8 Hz to detect LFEs beneath southern Vancouver Island; broadband stacks of nearly co-located LFEs (all the members of the same LFE family) still show a duration of only ∼0.3–0.5 s, a duration that moreover was found to be nearly independent of seismic moment M_0 (duration proportional to $\sim M_0^{0.1}$, over a range in M_0 of about one order of magnitude, with M_0 defined by the maximum of the displacement power spectrum between 0.5 and 1 Hz). In Guerrero, Farge et al. (2020) found similar durations (corner frequencies of ∼2 Hz) and moment-duration scaling, again over a range of about one order of magnitude in moment, although these LFEs were initially detected using a much narrower, 1–2 Hz passband. One question left unanswered by all these analyses is whether the observed clustering of durations is really an intrinsic feature of LFEs, or if it is biased by the narrow passband used to detect them.

The frequency band with a good signal-to-noise ratio for tremor detection is quite limited. The significantly reduced amplitude at high frequency makes the upper limit no higher than 10 Hz. The lower limit is usually around 1 Hz because of the strong interference from the microseismic noise between 0.1 and 1 Hz (Beroza & Ide, 2011). This narrow band of observation makes it possible to question the physical significance of what the community terms LFEs (Ide, 2008, 2010). Ide (2019) used a narrow-band template to detect "LFEs" in synthetic broadband random time sequences, and argued that what are called LFEs might just be an artifact of observing a broadband slow earthquake process over a narrow frequency band. He further showed that the broadband stacked templates of Bostock et al. (2015) actually include longer-period energy, up to periods of 4 s, in phase with the higher frequencies used to detect the LFEs, that are absent from the "LFEs" detected in his broadband random noise. However, the presence of this longer-period energy in the stacked templates from southern Vancouver Island does not by itself establish whether this longer-period energy reflects a longer-duration process associated with each LFE source; if it arises from the superposition of multiple LFEs, each relatively narrow-band, concentrated in time within a few seconds of the LFEs contributing to the stack; or if it is just a slightly longer-period part of a broadband process extending from "LFE" frequencies of a few Hz to much longer periods (Masuda et al., 2020).

At frequencies below the microseismic band, e.g., 0.02–0.05 Hz, very low-frequency earthquakes (VLFs) have been observed in both Japan and Cascadia (e.g., Ghosh et al., 2015; Ito & Obara, 2006; Ito et al., 2007; Obara & Ito, 2005). In Cascadia, Hutchison and Ghosh (2016) found VLFs during the 2014 ETS episode

that occurred when and where there was no strong tremor, and suggested that VLFs and tremor may result from asperities of different sizes or characteristic behaviors. However, Gomberg et al. (2016) questioned the reliability of these VLF detections, and used synthetic seismograms to show that the distinguishing characteristics of VLFs could be produced just by a collection of temporally clustered LFEs. Thus, the question of whether VLFs represent an independent feature along the broadband "slow earthquake trend" (Ide, Beroza, et al., 2007), or just a superposition of LFEs, appears to remain open. Other observational studies have attempted to broaden this question by more fully characterizing the moment-duration relation for events along the slow earthquake trend into the geodetic regime (e.g., Frank et al., 2018; Hawthorne & Bartlow, 2018).

In contrast to studies of VLFs, relatively few studies have focused on the portion of the spectrum between LFEs and the microseism band. Kaneko et al. (2018) were the first to identify individual slow earthquakes in the 0.1–1 Hz passband between LFEs and VLFs. They found that although the locations of detections in the 0.1–1.0 Hz passband appeared to be shifted from those in the tremor band of 2–8 Hz by ∼20 km, the 20 events they found in the 0.1–1 Hz band were too few, and their location uncertainty too large (the semi-major axis of their 1σ error ellipse is ∼10 km), to confirm the spatial separation of the different sources above the 2σ significance level. Thus, their locations in the two passbands still permit the interpretation that tremor consists exclusively of LFEs, with the longer periods being due to the relative timing of those LFEs.

We have found that data from the Canadian seismic network sometimes have sufficient signal-to-noise ratio to allow the detection of coherent tremor down to 0.5 Hz, above the strongest portion of the microseismic band but below the lower limit typically employed for tremor detection. Figure 1 shows some examples of tremor detected with a method similar to that of Peng et al. (2015), but using a passband of 0.5–1.25 Hz (referred as "LF", for "lower-frequency", hereafter). These data come from the PGC-SSIB-SILB trio of stations focusing around LFE family 002 of Bostock et al. (2012) (see Appendix B for details of the detection procedure). The upper panel of each subplot shows the detected 16-s-long LF signal, and the lower panel shows the same time window but filtered using a more typical tremor passband (1.25–6.5 Hz; "HF" hereafter). Figures 1a and 1b show one kind of LF signal, where a relatively isolated pulse-like arrival is highly correlated between the three stations in both the LF and HF passbands (after alignment around that pulse). But more commonly, we see a different kind of signal, as in Figures 1c and 1d, where both the LF and HF passbands are less dominated by a single arrival, and where the maximum amplitudes in the HF band need not coincide in time with those in the LF band.

In this paper we detect and locate tremor in these separate LF and HF passbands, to place constraints on the origin of the longer-period signal in tremor; that is, signal that occurs at lower frequency than the standard tremor passband. If tremor consists exclusively of LFEs, that is, if any contribution to the longer-period energy is just due to the timing of LFEs, then contemporaneous HF and LF detections should be almost co-located. In contrast, if LF and HF detections occupy clearly separate locations, it seems more likely that the LF energy has a source other than just the timing of LFEs. In Section 2 we introduce the data processing steps and provide a brief summary of our analysis method. Then in Section 3 and the Supporting Information S1 we describe how we use LFE templates to correct for the apparent differences in LF and HF source locations that arise just by virtue of filtering the data in the different passbands (what we call the "filtering effect" here). In this step we make use of the assumption that the relatively low- and high-frequency energy in the LFE templates comes from the same physical location on the fault, at least when averaged over many LFEs by stacking the members within each family.

In Section 4 we show that in general, the LF and HF sources come from roughly the same regions of the subduction interface, so in Sections 4 and 5 we next search for systematic offsets between the locations of contemporaneous LF and HF detections relative to the propagating fronts of RTMs. To guard against possible errors in our empirical filtering effect corrections, we focus on a region of the interface that hosts RTMs propagating in nearly opposite directions. We find that the LF energy appears to occur roughly 0.5 km farther behind the propagating fronts of RTMs than the HF energy, whether those fronts propagate to the ENE or to the WSW. For the RTMs occupying the same portion of the fault that do not propagate to opposite directions, the lagging distance could also be made consistent at a value of 0.6 km, for a systematic error across all filtering effect corrections of only 15%–20% of the measured corrections. This 0.5–0.6 km is small compared to the location error of individual LF detections, but the result seems to be robust owing to the

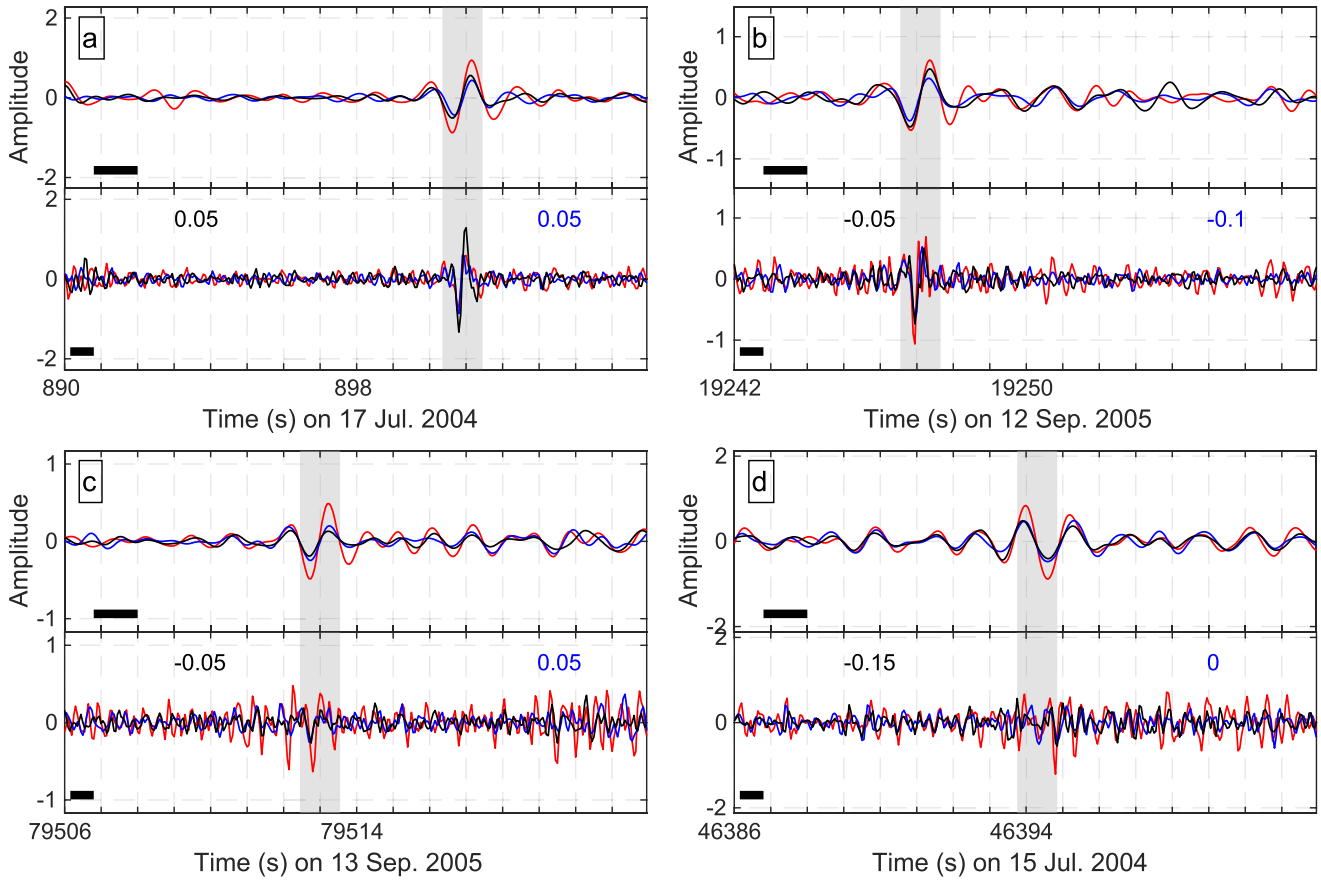

Figure 1. Examples of 16-s-long tremor detections in the LF (0.5–1.25 Hz) passband using the PGC-SSIB-SILB detector around LFE family 002 of Bostock et al. (2012). Appendix A explains how the waveform being plotted is derived from the horizontal velocity components corrected for shear-wave splitting and rotated into the optimal shear-wave particle motion direction. The upper panel of each subplot shows the detection in the LF passband. The records at stations SSIB (blue) and SILB (black) are aligned with respect to the reference station PGC (red), using the time offsets that maximize the summed cross-correlation coefficients. Tick mark spacing is 1 s. The lower panels show the same general time windows in the HF passband (1.25–6.5 Hz), but aligned independently. The numbers in blue and black are the differences in time offsets between the LF and HF bands that are needed to align the records at station pairs PGC-SSIB and PGC-SILB, respectively. The black horizontal bars denote the frequency bands in terms of period. The vertical gray area indicates the time window δt_{min} over which the arrival in LF has the most energy as defined in Equation B1. (a) and (b) show one kind of LF signal, where a relatively isolated pulse-like arrival is highly correlated between the three stations in both the LF and HF passbands. The HF records are aligned based upon a 4-s segment around that pulse. (c) and (d) show a more common signal, where both the LF and HF passbands are less dominated by a single arrival, and where the maximum amplitudes in the HF band need not coincide with those in the LF band. The HF records are aligned based upon the whole 16-s window.

large number of detections. If this result stands, it suggests that tremor consists of more than just a collection of LFEs, with longer-period energy being produced farther behind the migrating fronts of RTMs, where slip speeds for crack-like or pulse-like rupture propagation are lower (e.g., Andrews, 1976; Heaton, 1990; Madariaga, 1976).

2. Data and Method

In this study we use continuous velocity records at permanent stations (3-letter names) and temporary POLARIS stations (4-letter names) from the Canadian National Seismograph Network (CNSN) located on southern Vancouver Island, Canada (Figure 2). Because most *P* arrivals are difficult to recognize, only horizontal north (N) and east (E) components are used. Data from the POLARIS project, which operated from 2003 to 2006, are down-sampled from 100 to 40 Hz for consistency with the permanent stations. We carry out some pre-processing steps such as linear trend removal and tapering of the daily records, and instrument response removal. We examine 23 days including three major ETS periods: 1–5 March 2003, 12–21 July 2004 and 11–18 September 2005. Following Armbruster et al. (2014), we detect and locate tremor

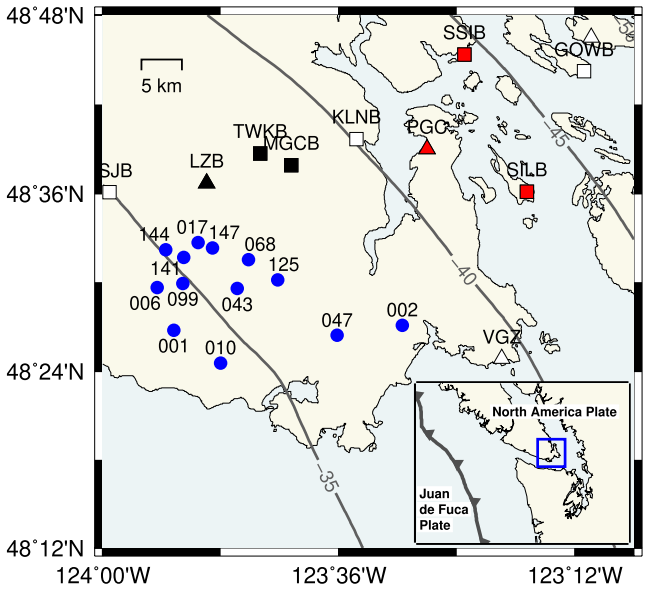

Figure 2. Distribution of station detectors on and LFE families beneath southern Vancouver Island that are used in this study. Triangles with 3-letter names represent permanent stations and squares with 4-letter names represent POLARIS stations. Stations within the PGC-SSIB-SILB detector are filled in red, those in the TWKB-LZB-MGCB trio are filled in black, whereas unused stations are left open. Blue circles and corresponding numbers are the 13 LFE families identified by Bostock et al. (2012) that were utilized in this study. Their locations are determined via the same method as tremor detections, by inverting the relative arrival times obtained via cross-correlation (in this case of the stacked LFE templates) at three stations using Hypoinverse (Klein, 2002), while forcing the families to be on the slab interface. Dark gray lines contour the slab interface geometry from McCrory et al. (2012) with a 5-km interval. The inset at the bottom right gives an overview of the study region (plate boundary from Bird [2003]).

using groups of three stations. The trio we emphasize here, TWKB-LZB-MGCB (Peng et al., 2015), images the areas surrounding 13 LFE families identified by Bostock et al. (2012) (Figure 2). We also used the 3-station detector PGC-SSIB-SILB (Rubin & Armbruster, 2013) to image the area surrounding LFE family 002 of Bostock et al. (2012), but found too few LF detections using that trio for it to be useful.

As in Peng et al. (2015), we rotate the horizontal components at each station into the dominant particle motion direction, after correcting for shear-wave splitting. The splitting parameters and particle motion directions are determined from preliminary LFE templates, made by stacking the broadband N and E records at each station using time windows determined from the LFE catalog of Bostock et al. (2012) and filtering the stacks using the passband 0.5–6.5 Hz (see Appendix A for details). We then refine the templates by cross-correlating the individual LFEs, already corrected for shear-wave splitting and rotated into the particle motion direction, prior to stacking (Appendix A). Hereafter, by "template" we mean these split-corrected, rotated, and refined stacks. We use these templates to correct for the apparent differences in travel time from one LFE source to the different stations that arise from the different passbands used (see next section). We use a 2-pole, 2-pass Butterworth bandpass filter throughout this paper if not specified otherwise. Data are filtered using the passbands 1.25–6.5 Hz and 0.5–1.25 Hz; we refer to these as the HF (high-frequency) and LF (low-frequency) bands hereafter. Tremor in the vicinity of each LFE family is detected using seismograms that are processed with the splitting parameters and particle motion directions determined from the templates for that particular family, and subsequently filtered into the HF and LF passbands.

To make the detections we employ a sliding time window with a fixed length (4 s for HF; 16 s for LF) and sliding step (1 s for HF; 8 s for LF) to cross-correlate the 3 station pairs (Rubin & Armbruster, 2013) (see Appendix B for details). To determine the general time offsets between stations for each LFE family we first cross-correlate the LFE templates of that family at the 3 stations, and we enforce a maximum possible lag around that expectation when cross-correlating the processed daily seismograms. A successful detection requires the maximum normalized cross-correlation (CC) coefficient, averaged over the 3 station pairs, to be higher than a threshold value (0.4 in HF; 0.35 in LF), and the circuit of three time offsets between the station pairs that achieve this maximum average CC coefficient to be small enough (absolute value less than 0.0375 s in HF and 0.2 s in LF). Given a successful detection, we then force the circuit of time offsets to be zero, and choose the two independent time offsets that maximize the average CC coefficient for the 3 station pairs (that must again be higher than the same threshold value).

Assuming that tremor is located on or near the plate interface (e.g., Armbruster et al., 2014; Brown et al., 2009; La Rocca et al., 2009, 2010; Shelly et al., 2006; Wech & Creager, 2007), these two independent time offsets are sufficient to determine the source location. To do so we use Hypoinverse (Klein, 2002) with the regional velocity model "Puget Sound P3" (Crosson, 1976), and iteratively force the source to locate at the depth of the plate interface according to the slab model Slab1.0 (McCrory et al., 2012). Because we expect the splitting parameters and dominant particle motion directions to vary spatially, HF detections more than 8 km and LF detections more than 12 km away from their parent LFE family are discarded. Even enforcing this criterion, some detections are connected to two or more parent LFE families; in such cases we adopt the single detection with the highest CC value. The catalog that results from merging those based on the 13 LFE families contains 51,057 HF detections and 18,491 LF detections. Most of the detections occur in spatially and temporally clustered bursts that correspond to rapid tremor migrations (RTMs); however,

some detections are isolated temporally or spatially and are likely false positives, while some that occur during RTMs may be mislocated because of cycle skipping.

To analyze the spatial offset between HF and LF tremor detections relative to the propagating fronts of RTMs, we first identify dominant RTMs that have a simple unidirectional migrating pattern using the HF catalog, which has more and more accurately located detections. By projecting both HF and LF detections onto the propagation direction of each migration, as determined by the HF catalog, we are able to analyze the average spatial relationship between contemporaneous HF and LF detections within a given migration. Before doing so, however, we must account for apparent spatial offsets between the HF and LF detections that result from the different passbands adopted.

3. Empirical Filtering Effect Correction

Because we are locating tremor detections in different frequency bands, we need to account for the possibility that apparent differences in source location may arise from the different frequency bands used, independent of any actual differences in location. We refer to this as the "filtering effect" in this paper. The filtering effect potentially contains multiple sources of perturbations to the travel time along any source-station path as measured in different passbands. These could include near-station or near-source reflections that change the shape of the arriving pulse (e.g., Nowack & Bostock, 2013), physical dispersion caused by intrinsic attenuation in which seismic waves of different frequencies travel at distinct speeds, or other factors we have not thought of. The time offsets we measure by cross-correlation potentially include this filtering effect.

To obtain tremor locations using a single passband, we rely on cross-correlation measurements to determine the two independent differential arrival times (travel times) between three stations 1, 2, and 3, which for the standard HF passband we write as Δt^H_{12} and Δt^H_{13}. Therefore, to correct for apparent location differences when using two different passbands, we are concerned with the difference in differential travel time between the two passbands, Δt^{L-H}_{12} $(\equiv \Delta t^L_{12} - \Delta t^H_{12})$ and Δt^{L-H}_{13}. To estimate this "differential" filtering effect, we assume that the LFE template includes relatively low- and high-frequency energy coming from the same physical location, at least when averaged over many LFEs by stacking the members within each family. We then filter the template at each station in the LF and HF passbands, to obtain Δt^{L-H}_{12} and Δt^{L-H}_{13} via cross-correlation. To increase precision, for these high signal-to-noise-ratio templates the data are temporarily up-sampled to 80 Hz. Just as when we locate each of our fixed-window-length detections, we cross-correlate the filtered templates at each station pair, and then obtain the time offsets that maximize the average CC coefficient while forcing the circuit of three time offsets $(\Delta t_{12} + \Delta t_{23} + \Delta t_{31})$ to be zero. The filtering and cross-correlation are done separately for the HF and LF passbands. The difference in time offsets for the different passbands represents the empirical filtering effect correction we are seeking.

Figure 3 illustrates this procedure using family 043. Figure 3a shows the normalized 10-s broadband velocity templates stacked according to the timings of LFEs in family 043 at stations TWKB, LZB, and MGCB. Using the appropriate corner frequencies results in the HF-filtered (Figure 3b) and LF-filtered (Figure 3c) templates. Figures 3d and 3e show the cross-correlation functions for the three station pairs in the two passbands. The open symbols mark the time offsets which maximize the individual CC coefficients (e.g., Δt_{12}). However, under the constraint $\Delta t_{12} + \Delta t_{23} + \Delta t_{31} = 0$, the accepted offsets, denoted by the closed symbols that maximize the summed cross-correlation of all three station pairs, are not necessarily the same as those from the individual CC measurements. The differences in the constrained offsets at station pairs TWKB-LZB and TWKB-MGCB between LF and HF are $\Delta t^{L-H}_{12} = -0.0875$ s and $\Delta t^{L-H}_{13} = -0.125$ s, respectively. This means that if one aligns the HF signals at the two stations, the LF signal arrives 0.0875 s later at station LZB than TWKB, and 0.125 s later at station MGCB than TWKB.

We determine the filtering effect, Δt^{L-H}_{12} and Δt^{L-H}_{13}, for each of the 13 families using the stacked LFE templates from that family via the same procedure. These Δt^{L-H} are then used to correct the measured LF time offsets for any LF detection tied to the family in question. That is, we adopt the measured delay times in the HF passband without alteration, but subtract Δt^{L-H}_{12} and Δt^{L-H}_{13} from the measured CC time offsets between station pairs, i.e., TWKB-LZB and TWKB-MGCB, for detections made in the LF passband. We find that the filtering effect correction is not sensitive to the length of the window used when cross-correlating the templates (Figure S1 in Supporting Information S1), suggesting that the cross-correlation functions are

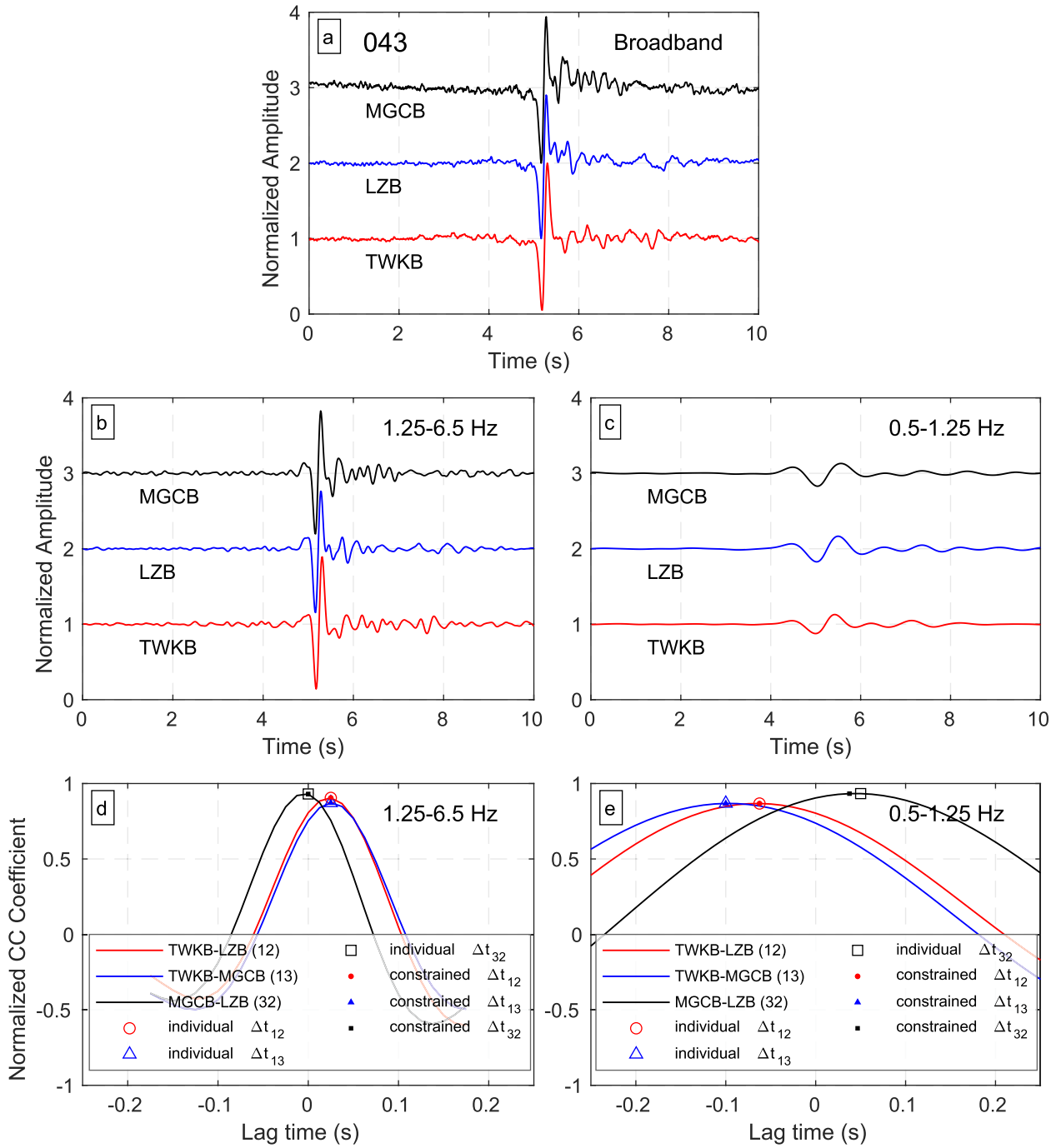

Figure 3. Filtering effect for detections tied to LFE family 043 using the TWKB-LZB-MGCB detector. (a) shows the stacked "broadband" velocity templates (corner frequencies of 0.04 and 20 Hz were used by the cosine pre-filter in removing the instrument response), sampled at 80 Hz. (b) and (c) are the filtered templates in the frequency bands 1.25–6.5 Hz (HF) and 0.5–1.25 Hz (LF), respectively. (d) and (e) are the normalized cross-correlation functions for the corresponding passbands. The open symbols mark the time offsets which maximize the individual CC coefficients between each of the three station pairs. The closed symbols mark the time offsets that maximize the summed cross-correlation of all station pairs under the constraint $\Delta t_{12} + \Delta t_{23} + \Delta t_{31} = 0$.

dominated by the main *S*-wave arrival rather than the coda. But for consistency, we adopt the same window length used when detecting and locating tremor (4-s for HF and 16-s for LF), centered roughly at the main arrival. The median of the circuits of the three individual time offsets for the 9 LFE families of primary interest (families listed in the inset to Figure 4), located in the northwestern portion of our study region, is about 0.003125 s at HF and 0.0125 s at LF. The filtering effect corrections determined from the same families

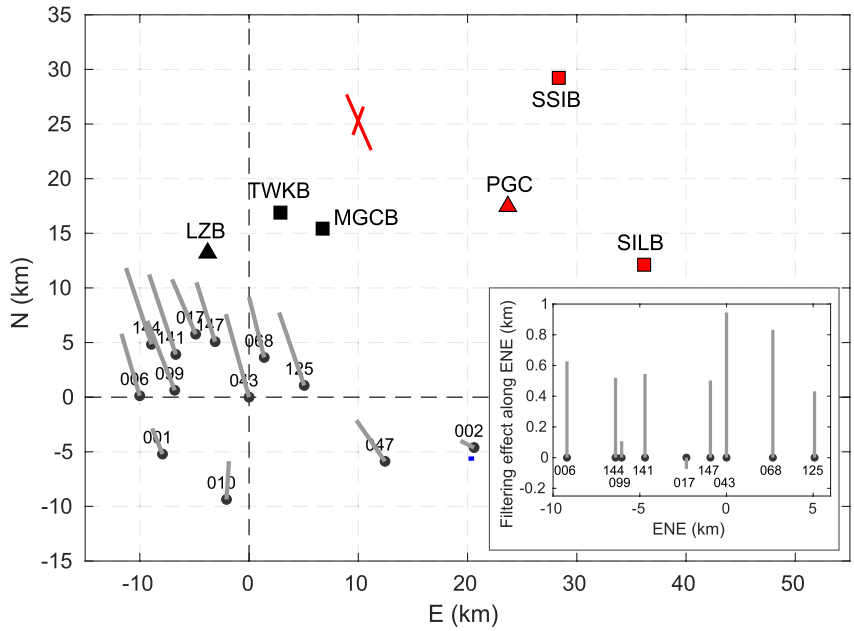

Figure 4. Apparent spatial offsets between LF and HF detections due to filtering in the two distinct passbands, plotted for all LFE families. The black dot at one end of each gray bar is the HF location of the LFE family as seen by the TWKB trio, while the other end of the gray bar is where the LF detection would plot if the filtering effect was not corrected for. Symbols for the LFE families and station trios remain the same as in Figure 2. The tiny blue bar near family 002 denotes the location difference for that family estimated using the PGC trio. The long and short axes of the red cross denote the location errors resulting from an error of ±0.05 s in the differential travel time between the station pairs TWKB-MGCB and TWKB-LZB, respectively, for LFE family 043 (black circle plotting at the origin). The bottom right inset plots the components of the filtering effect along the ENE-WSW direction, roughly parallel to the propagation direction of most of the RTMs we use, for the 9 LFE families in the northwestern portion of the imaged region.

are typically larger than 0.0625 s. If we adopt the median circuit of the individual time offsets as a crude empirical measure of the uncertainty in our filtering effect correction, then this uncertainty amounts to only one-fifth of the filtering effect. We note finally that for the 9 LFE families of primary interest, the difference between the median time offsets of contemporaneous HF and (corrected) LF detections tied to that family are often small, compared to the corrections themselves (Figures S2 and S3 in Supporting Information S1). This is despite that the vast majority of these detections do not contribute to the stacks used to determine the filtering effect corrections.

To visualize these time offsets in terms of a spatial offset in the vicinity of each LFE family, we assume there is a HF detection denoted by offsets (0,0), that is, at the HF location of that family, and then convert the differential offsets Δt_{12}^{L-H} and Δt_{13}^{L-H} into absolute locations using Hypoinverse (Klein, 2002), as if they represent a LF detection. The resulting spatial offsets for the TWKB trio are shown in Figure 4. One end of each gray bar (black dot) is the HF location of the LFE family, while the other end is where the LF detection would plot if the filtering effect were not corrected for. The first point to note is that these offsets are quite large–typically more than 5 km for the 9 LFE families in the northwestern portion of the imaged region. This is an order of magnitude larger than the systematic spatial offset we find between the LF and HF detections after correcting for the filtering effect, raising the possibility that modest errors in our empirical filtering effect corrections could significantly influence the results. For this reason, in the analysis to follow we focus on regions of the subduction interface that host RTMs propagating in nearly opposite directions. That is, if the apparent LF–HF offset from the same portion of the fault varies systematically with respect to the fronts of RTMs propagating in opposite directions, it cannot be ascribed to errors in our filtering effect corrections. The second point to note is that the filtering effect corrections are regionally consistent, in that the corrections for nearby families are similar in amplitude and direction. This gives us some confidence that, whatever the source of the filtering effect, our approach to determining it is robust, and, importantly,

that the LF–HF offsets of sources that lie between LFE families will not be heavily dependent on which family is used to correct for the filtering effect. We test this assertion more systematically in Section 5.

In the Supporting Information S1 we show that the filtering effect we see cannot be explained by physical dispersion due to spatially uniform, frequency-independent attenuation alone. A uniform shear-wave quality factor Q_s of 200 (Gomberg et al., 2012) results in a filtering effect roughly an order of magnitude smaller than we observe (a few thousandths of a second, compared to the observed amplitude of a few hundredths of a second). Amplitudes of a few hundredths of a second would require values of Q_s closer to 20, unreasonably low for a path-averaged value. Moreover, in a uniformly-attenuating body LF energy will lag HF energy by an amount that increases monotonically with propagation distance, which is inconsistent with our observations. The phase lag as a function of frequency, as determined from the phase of the cross-spectrum between LFE templates, does not simply manifest as a constant time offset between the different frequency ranges (Figures S4 and S5 in Supporting Information S1). Therefore the filtering effect measured by cross-correlating the templates in the time domain is likely an average offset between the different passbands used. The theoretical prediction from physical dispersion also fails to explain the observed phase lag as a function of frequency. Values of Δt^{L-H} of a few hundredths of a second are more likely due to subtle variations in the shape of the pulse-like arrival, due perhaps to near-source or near-station velocity structure.

Note that the large apparent spatial offset between HF and LF sources in Figure 4 can be explained by the small aperture of the TWKB trio in the NW-SE direction (a few km). Figure 4 shows the filtering effect for LFE family 002 using both the TWKB (gray bar) and PGC (blue bar) trios. The difference in differential travel times are comparable (for the PGC trio, $\Delta t_{12}^{L-H} = -0.0125$ s and $\Delta t_{13}^{L-H} = -0.0375$ s; for the TWKB trio, $\Delta t_{12}^{L-H} = 0.025$ s and $\Delta t_{13}^{L-H} = -0.0375$ s), but the smaller station spacing of the TWKB trio in the NW-SE direction transforms this comparable time difference into a much larger location difference (see also Figure S6 of Peng et al., 2015). The long axis of the red cross in Figure 4 shows the location error due to an error of ±0.05 s in the differential travel time between the station pair TWKB-MGCB for LFE family 043 (located at [0,0] in the plot), whereas the short axis shows the location error from the same differential timing error between the station pair TWKB-MGCB. Given the location error ellipse, the major orientation of the filtering effects mainly comes from the small aperture of the TWKB-LZB-MGCB trio in the NW-SE direction, rather than a large difference between the two time offsets from the two station pairs, Δt_{12}^{L-H} and Δt_{13}^{L-H}.

4. RTM Propagation Directions

The bulk of the detections in our "standard" tremor catalog (HF, in the notation of this study) occur during tremor bursts that, after detection and location, manifest as rapid tremor migrations. The tremor sources occupy patchy regions on the fault, with the same regions being activated by numerous RTMs within each ETS episode (Rubin & Armbruster, 2013; Peng et al., 2015). In both passbands, there are detections that are isolated in space and time; these seem likely to be false positives. For those detections that are clustered in space and time, and therefore likely to be real seismic sources, we find that the LF detections occur at roughly the same time and (after applying the filtering effect corrections) at roughly the same location as contemporaneous HF detections. We find that very few RTMs are visible in the 0.5–1.25 Hz (LF) catalog in 2003, probably because this was the only one of the 3 ETS events to occur during winter (March), when the noise level in the microseismic band is typically higher. From the cumulative density map of the HF and LF tremor catalogs from the ETS episodes in 2004 and 2005 (Figure 5), it seems that regions that generate most HF and LF energy are generally the same. This need not be the case; for example, one could imagine that LF detections might be concentrated in regions adjacent to HF tremor patches, or that RTMs seen in the HF catalog are preceded or followed by LF detections. Although there are a few regions in Figure 5 where there are a relatively larger number of LF detections compared to HF (e.g., a N–S band centered near −2 km E and −5 km N) or vice-versa (e.g., a NNW-SSE band centered near the origin), we do not highlight these regions here for several reasons. These include the larger location error in the LF catalog, possible errors in the filtering effect corrections in regions between the 13 LFE families used to determine them (e.g., the N–S band centered near −2 km E and −5 km N is between the family 043 and 010 whose filtering effect corrections are quite different), and the distortion of locations at distances far away from the TWKB detector (e.g., in the far SE quadrants of these maps). Establishing that these modest variations in location reflect source processes requires additional investigation of the space-time history of both the detections and the overall

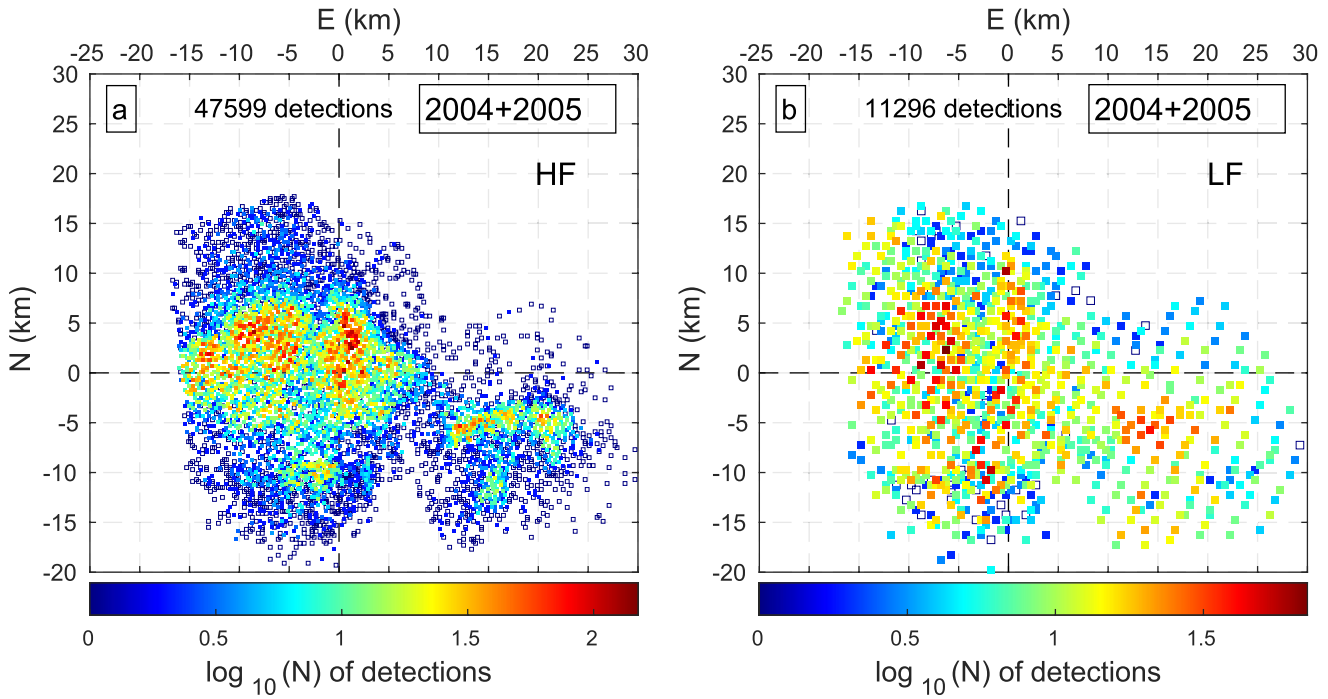

Figure 5. Cumulative density map of the HF and LF tremor catalogs from the ETS episodes in 2004 and 2005 identified using the TWKB trio. (a) and (b) are the density maps for the HF and LF detections, respectively. A distance cutoff of 12 km from their parent family is used for both LF and HF detections here. Each 200 × 200 m (HF) or 500 × 500 m (LF) bin is color-coded by the logarithmic number of detections within it. Unfilled bins mean there is only one detection inside. The total number of detections is given at the top.

seismic energy of the two passbands that is beyond the scope of this paper. Here we test the hypothesis that the LF and HF detections have systematic offsets relative to the propagating fronts of RTMs, even while the regions of the fault that produce HF and LF energy are strongly overlapping.

We identify RTMs using the HF catalog because the signal-to-noise ratio is higher within this passband, and because its wider range of frequencies and higher-frequency content permit more accurate relative arrival time measurements (and hence relative locations) even for the same signal-to-noise ratio. We focus on migrations that have a simple unidirectional propagation direction. First, we sequentially group the HF detections that occur less than a threshold time $t_{thr} = 1 \times 10^{-3}$ days (i.e., 86.4 s) after the preceding detection into a tremor burst (Figures S6 and S7 in Supporting Information S1). Only bursts that have at least $n_{thr} = 15$ detections in both the HF and LF catalogs are included. This automatic temporal clustering algorithm (Peng & Rubin, 2017; Wu et al., 2015) does not ensure that the detected tremor bursts are also clustered in space with a unidirectional pattern. To ensure that this is the case, we examine all the detected bursts in map and space-time plots, and modify the automatically-detected time ranges for ~25% of the bursts (additional details are given in the Supporting Information S1, and some examples are shown in Figures S8–S10 in Supporting Information S1). Many of these bursts propagate in a well-defined direction for distances that range from 5 to 20 km.

To determine these propagation directions and apply some additional quality-control measures, for each burst we next carry out a regression analysis, which we describe with the help of one migration on 16 July 2004 shown in Figure 6. First, we search over a series of trial propagation directions, onto which all HF detections are projected, and consider these projected locations as a function of time. We then implement a robust least-squares regression that minimizes the weighted distances of these projected locations to a best-fitting line (i.e., the weighted root mean squared error, RMSE), using a bisquare weighting scheme (e.g., Holland & Welsch, 1977). The bisquare method iteratively downweights detections that are distant from the main cluster; in principal these could represent isolated false positives, or clustered true detections that happen to be distant from the RTM of interest. To choose which migrations should be kept for analysis we need some measures for the quality of the determined propagation direction and for the unidirectionality

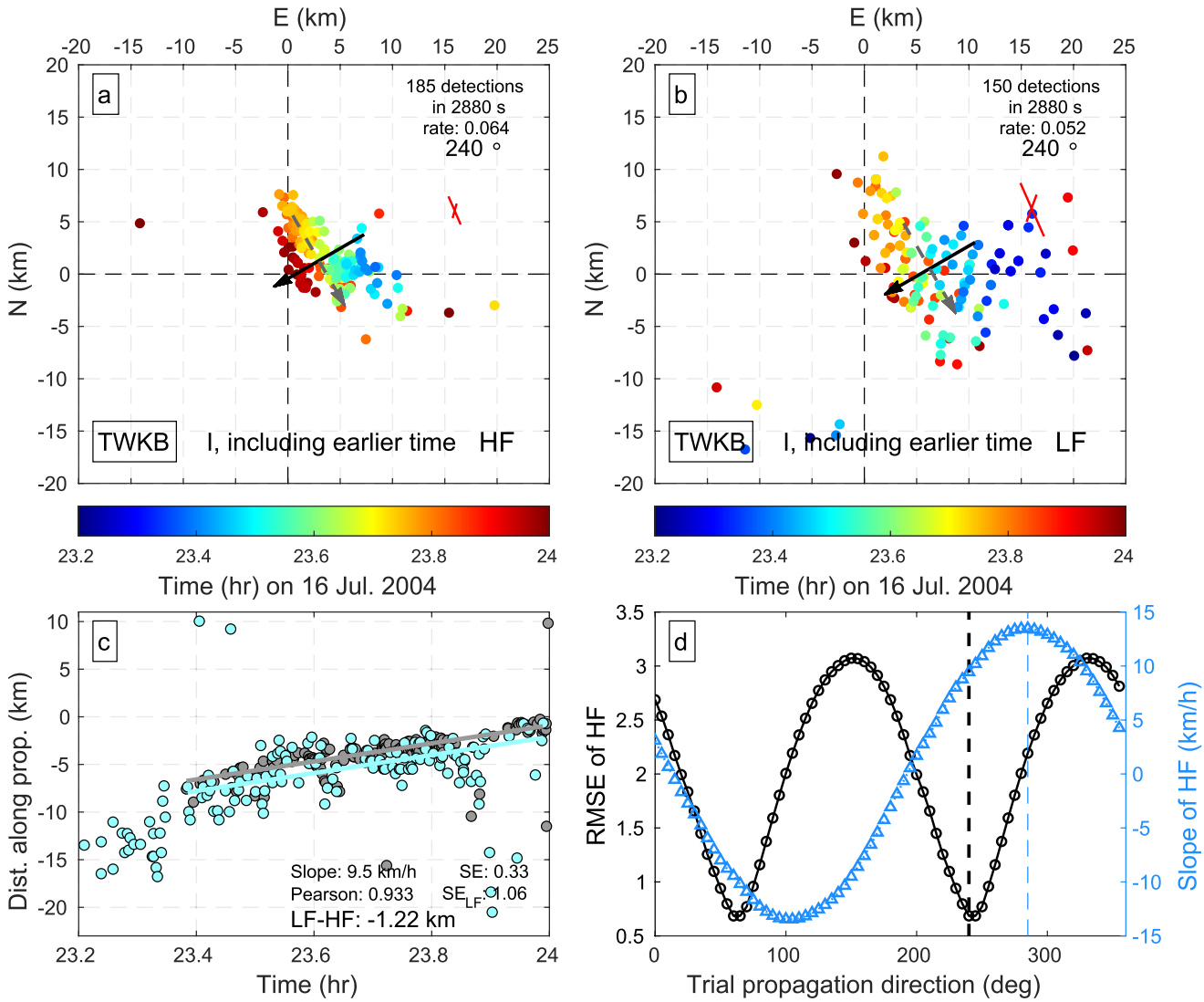

Figure 6. Regression analysis of the RTM detected using the TWKB trio that occurred from 23.4 to 24 h on 16 July, 2004, labeled as I in Figure 8a. We extend the automatically-determined window to 23.2 h only for illustration, to show earlier LF detections which are spatiotemporally consistent with the later ones. (a) and (b) are the RTM in the HF and LF catalogs, color-coded by time. Solid black and dashed gray arrows indicate the propagation direction and its orthogonal. The long and short axes of the red cross show the location errors due to an error of ±0.025 s (a) or ±0.05 s (b) in the differential travel time between the station pairs TWKB-MGCB and TWKB-LZB, respectively, for the representative LFE family 043. (c), the projections of HF (gray circles) and LF (cyan circles) detections onto the propagation direction. The gray line is the best-fitting line for HF projections, in which both the slope (propagation speed) and intercept are inverted for. Assuming the LF detections have the same propagation direction and speed, we invert for only the intercept of the cyan line. SE: Standard error of the slope of the HF fitting. Pearson: Pearson correlation coefficient of the HF fitting. SE_{LF}: Standard error of the slope of fitting the LF detections. LF–HF: Difference between the vertical intercepts of the fitted lines. (d), the variation of the resulting weighted root mean squared error (RMSE) and the propagation speed from the regression using each trial direction. The black and blue dashed lines mark the minimum-RMSE and maximum-speed directions, respectively, one of which is bold if chosen as the propagation direction. In most cases the minimum-RMSE direction is preferred, as is the case here.

of the migration. Our default is to accept migrations in which the standard error of the slope of the linear fit to the projected HF locations vs. time (gray line in Figure 6c) is smaller than 3 km/h, and for which the Pearson correlation coefficient (e.g., Benesty et al., 2009) between the projected HF locations and time is simultaneously larger than 0.5, from the regression using the trial propagation direction that minimizes the resulting weighted RMSE among all trial directions (minimum-RMSE direction hereafter; dashed black line in Figure 6d).

We adopt the minimum-RMSE direction as our default propagation direction because, given the long axis of the location error ellipse, the minimum-RMSE direction is the best option for measuring a reliable spatial

offset between the projections of LF and HF detections onto the estimated propagation direction. The HF and LF detections in any RTM would be subject to location error ellipses with the same orientations but different magnitudes (larger for the LF detections), with location errors being skewed toward the long axis of the error ellipse, regardless of the true propagation direction. For the example in Figure 6a, the minimum-RMSE direction is nearly perpendicular to the long axis of the error ellipse (red cross), with the possible implication that this direction is biased by that location error (the true propagation direction might be more nearly east-west, for example). For this particular migration that does not appear to be the case, however, in that the overall width of the propagating front in the orthogonal direction (the direction of the gray dashed arrow) is larger than the distribution of locations in narrow time windows (orange and darker blue dots, for example, which give a better sense of the upper bound on the location error in that direction). For this example the propagation direction happens to be roughly in the direction of the short axis of the location error ellipse. This is common; the main tremor front in these slow slip episodes propagates more-or-less along the strike of the subduction zone, and many RTMs propagate along the main tremor front; that is, close to the dip direction (Peng et al., 2015), which because of the mostly along-dip design of the POLARIS array is roughly parallel to the short axis of the error ellipse.

One can imagine scenarios in which the minimum-RMSE direction could lead one astray. For example, if there is a narrow, linear migration of sources (e.g., from east to west) in which the distribution of sources in any small time window is more elongate in the propagation (E–W) direction than the orthogonal (N–S) direction, even after the addition of location errors, then the minimum-RMSE direction will be oriented N–S, perpendicular to the true direction. None of the migrations in our catalog have this character; however, as an additional check for robustness, for each tremor burst we also consider the trial propagation direction that maximizes the slope of the best-fitting line to the projected HF locations. This maximizes the propagation speed (we call this the maximum-speed direction hereafter), and it would capture the proper direction in the above hypothetical scenario. In Figure 6d the minimum-RMSE and maximum-speed directions differ by roughly 45°. Using the maximum-speed direction (blue dashed line in Figure 6d) would lead to a LF–HF offset of −1.8 km rather than − 1.2 km. Although the "true" propagation direction might be somewhere between the two, if the location errors in the direction of the long axis of the error ellipse are as small as those suggested by the detections with similar colors in Figure 6a, the maximum-speed direction is spurious and the resulting LF–HF offset when projected onto that direction is more prone to errors. In this example the default, minimum-RMSE direction (dashed black line in Figure 6d) is adopted as the propagation direction (black arrow in Figure 6a).

Based on examination of all the HF migrations, we adopt the minimum-RMSE direction as the propagation direction unless the Pearson correlation is increased by at least 0.05 using the maximum-speed direction. This occurs only 5 times in total; one example is shown in Figure C4. There is one exceptional case (Figure S11 in Supporting Information S1) for which the adopted propagation direction is the minimum-RMSE direction obtained from fitting the LF migration, because the resulting standard error of the slope of fitting the LF detections (SE_{LF}) is smaller than, and the Pearson correlation is larger than, those obtained using either the minimum-RMSE or maximum-speed directions of the HF detections. More discussion concerning the selection of eligible migrations and their propagation directions, as well as how the measured LF–HF offset varies with the choice of propagation direction of each migration, is given in the Supporting Information S1. We also discuss the effect of the choice of propagation direction on the average LF–HF offset in Section 5.

Ultimately we preserve 52 migrations out of the initial 158 tremor bursts determined automatically using the TWKB trio. We order all the 52 migrations spanning the ETS episodes in 2004 and 2005 chronologically and refer to them by their sequential numbers. Note that though one RTM in the vicinity of LFE family 002 passes all quality measures, we do not trust it because this region is generally not imaged well due to the possible distortion of locations (e.g., Figure S2 of Peng et al. (2015), and Figures S12 and S13 in Supporting Information S1).

As the LF detections (Figure 6b) are generally fewer in number and have larger location errors, we assume that they have the same propagation direction (black arrow in Figure 6b) and propagation speed (slope of the cyan line in Figure 6c) as was determined for the HF detections. This means that the sole parameter we invert for using the LF locations with the bisquare weighting is the intercept of the cyan line in Figure 6c, and that the vertical separation between the gray and cyan lines reflects the average separation between

the LF and HF detections in the RTM propagation direction. This separation is taken to be the difference between the vertical intercepts LF–HF of the fitted lines in Figure 6c, with negative values meaning that on average the LF detections lag the HF detections (the LF detections occur later at a given location, or at a given time are located behind the RTM front as determined by the HF detections).

Note that the migration plotted in Figure 6 includes a 0.2-h period of time prior to the automatically-determined time window from 23.4 to 24 h, because the LF detections start earlier than the HF detections in this particular migration (this is seen most clearly in Figure 6c). The earlier LF detections are spatiotemporally consistent with the later LF and HF detections such that they are unlikely to be false positives. The earlier LF energy from 0 to 5 km N also seems to come from a region where there is a relative deficit of HF energy compared to LF (Figure 5). But due to the several reasons mentioned previously, we are not yet willing to conclude that this region produces LF energy only. Another possibility is that when this portion of the fault is active it is active over a larger region, such that longer-period energy correlates better than shorter-period energy, or that because of path effects longer periods correlate better between the 3 stations. Nevertheless, the automated window succeeds in capturing the period with roughly contemporaneous HF and LF detections that should be included in the regressions. For the migration in Figure 6 we use the automated time window (shown by the gray and cyan lines in panel c); we show the longer window only for illustration.

5. Spatial Offsets Between LF and HF Detections

The offset between the LF and HF detections in Figure 6, about −1.2 km, is larger than average. Most offsets are on the order of a few hundred meters, which is smaller than both the estimated location errors of the LF detections in Figure 6b, and the size of the filtering effect corrections in Figure 4. The former difficulty can be surmounted by averaging over enough detections from several migrations, and to a large extent this is the philosophy behind using simple linear fits to the projected tremor locations vs. time in each migration (e.g., Figure 6c). However, averaging many locations will not compensate for any systematic errors in the empirical filtering effect corrections. That these corrections appear spatially coherent (Figure 4) gives us some confidence that they are smoothly varying and reasonably well determined; however, they are large enough that it is not difficult to imagine that modest errors in these corrections could bias the LF–HF offsets in multiple migrations.

To circumvent this potential difficulty, we search for regions of the subduction interface that host migrations propagating in different, and ideally nearly opposite, directions. Our reasoning is that if (for example) LF detections are apparently consistently located to the SW of HF detections for migrations that propagate to the NE, but NE of migrations in the same region that propagate to the SW, then these apparent offsets cannot be ascribed to time-independent errors in the filtering effect corrections, as the same corrections are being applied in both cases.

To find regions that host opposing migrations, we examine in map view the propagation direction and areal extent of all 52 recognized migrations as seen in the HF catalog (Figure S14a in Supporting Information S1). The highest density of nearly-oppositely-propagating migrations is located in the northwestern part of our study area, and hence we focus our attention here. The propagation direction of most of these opposing RTMs is close to perpendicular to the orientation of the filtering effect corrections (Figure 4), which fortunately means that the errors in the filtering effect corrections in this direction are likely the smallest. As the orientation of the filtering effect corrections is (not coincidentally) close to parallel to the long axis of the location error ellipse, the location errors are also the smallest in this direction. We don't trust the remaining opposing migrations (one SE-NW pair and one SSW-NNE pair; Figure S14 in Supporting Information S1) since their propagation directions are more nearly parallel to the filtering effect corrections and the long axis of the location error ellipse.

Ultimately, we are concerned with the systematic location offset LF–HF between the HF and LF detections as projected onto the propagation direction of the RTM, so ideally this offset would be relatively insensitive to the choice of propagation direction. However, for many RTMs this is not the case. The LF–HF offset being sensitive to the propagation direction is not necessarily problematic; as discussed earlier, for many RTMs we have strong reasons for preferring the minimum-RMSE direction. Nonetheless, in some sense the sensitivity of the measured LF–HF offset to propagation direction is a measure of the robustness of

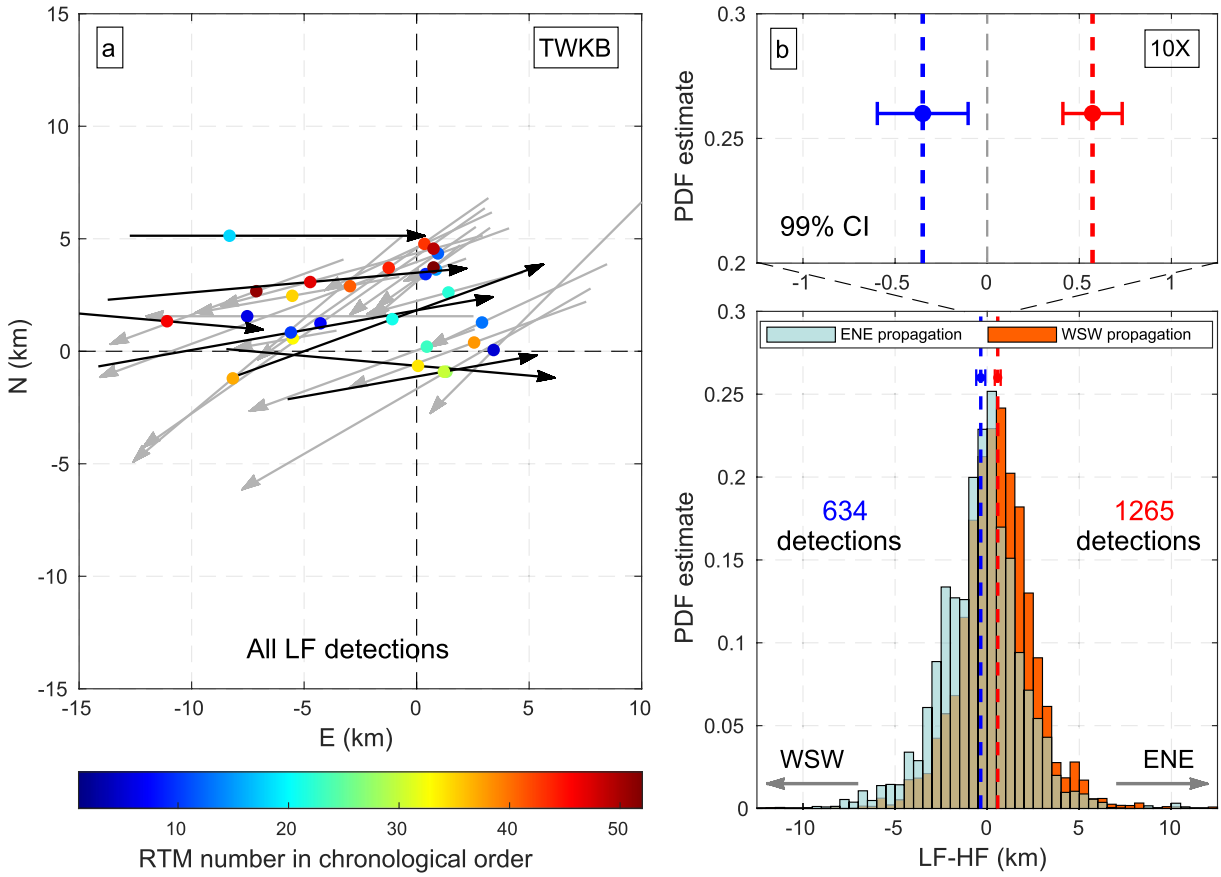

Figure 7. Significance of the difference between the mean (LF–HF) offsets of the WSW- and ENE-propagating migration groups in the northwestern portion of our study area. (a) shows the selected RTMs, where the black and gray arrows represent the propagation direction and extent of the migrations in the ENE-propagating group and WSW-propagating group, respectively. Each solid circle represents the median location of the HF detections, color-coded by the sequential number of that migration. The lower panel of (b) plots the histograms of the LF–HF offsets for the WSW- (cyan) and ENE-propagating (orange) groups. The height of the histogram is normalized to its PDF estimate. The vertical dashed lines represent the (bisquare-weighted) sample means of the offsets for the two groups, which are about 570 m and −350 m, making a difference of 920 m. The error bar centered at the sample mean is the 99% confidence interval of the mean. The upper panel of (b) shows a zoom of these non-overlapping confidence intervals.

our method. In some cases, large differences in offset result from large differences in the two potential propagation directions (Figure S15 in Supporting Information S1); in some cases they come from relatively poor fits to scattered LF detections. If the fit to the LF detections is poor and the difference in LF–HF offset between the two potential propagation directions is small, keeping that migration would not bias the offset estimate; but if the difference in offset is large, we might want to throw that migration out even if we trust one of the potential propagation directions more than the other. To guard against the least robust of our measurements, we discard from the nearly-oppositely-propagating migrations those for which the difference in offset between the two possible directions is larger than 1 km, and for which the standard error of the slope of the linear fitting to the LF detections (SE_{LF}) is simultaneously higher than 3 km/h (determined empirically). We recognize that this somewhat arbitrary choice for discarding migrations could be a source of bias in the following spatial offset analysis, so later in this section we explore how varying this threshold influences our results.

Eventually, we find 27 eligible RTMs that propagate in the northwestern portion of the study area in nearly opposite directions, and we separate them into WSW-propagating and ENE-propagating groups, with respectively 20 and 7 members. The chosen migrations are illustrated in Figure 7a, where the arrows represent the propagation direction and extent of the HF migrations in the WSW-propagating (gray) and ENE-propagating (black) groups. Each solid circle represents the median location of the HF detections, color-coded by the sequential number of that migration. As an additional check, Figure S16 in Supporting Information S1

plots the cumulative density map of the HF and LF detections belonging to the migrations in each of the ENE- and WSW-propagating groups. To a large extent these opposing migrations occupy the same portion of the fault, so any errors in the filtering effect corrections should affect the LF–HF offsets of the WSW- and ENE-propagating groups similarly.

To analyze the statistics of the two groups, we treat each LF detection as an independent measurement, and take the vertical distance from each LF detection to the fitted HF line (see Figure 6c) as the spatial offset (LF–HF) in the propagation direction. To place the offsets from the two different groups into the same geographical coordinate frame, we need to assign a common sign convention to these offsets. We define an offset to be positive if the LF detection is located ENE of the linear fit to the HF detections at that time, so that (for example) if on average the LF detections lag the HF detections, the average offset would be positive for migrations to the WSW, as in Figure 6c, and negative for migrations to the ENE. We then combine all the offsets for each of the WSW- and ENE-propagating groups into a single histogram for that group. Each datum (that is, each distance measurement from an LF detection to the fitted HF line for that RTM) contributes to the histogram by an amount equal to its weight (0–1) assigned by the bisquare regression for the intercept of the LF migration.

The resulting histograms for the two groups are shown in the lower panel of Figure 7b, with the number of measurements for each group indicated. The height of each histogram is normalized to its probability density function (PDF) estimate. The vertical dashed lines represent the (bisquare-weighted) sample means of the offsets for the WSW- and ENE-propagating groups, which are about 570 m and −350 m, respectively. The error bar centered at the sample mean is the 99% confidence interval of the mean, which is computed following Equation 4.46b of Bendat and Piersol (2011). The upper panel of Figure 7b shows a zoom of these non-overlapping confidence intervals. We do not interpret the width of these distributions because we suspect that this width is dominated by the LF location errors (a Gaussian fit to the data gives a weighted standard deviation σ of $\sim$2 km). However, if one treats the samples in these histograms as independent (a point we return to below), it is clear that the average location difference between the LF and HF detections is significant. Moreover, since these opposing migrations occupy roughly the same portion of the fault (Figure S16 in Supporting Information S1), any error in the empirical filtering effect corrections would impart the same shift to both distributions in Figure 7b. Consequently, even if the mean offset of either group is subject to uncertainty larger than the indicated confidence intervals, the difference between the two means is largely independent of any error in the filtering effect correction.

To further quantify the significance of the non-overlapping confidence intervals in Figure 7b, we carry out a Student's t-test (Press et al., 2007) on the two distributions assuming the true population variances are unknown (although they appear to be quite similar). The probability (p-value) of the null hypothesis that the two distributions have equal means, so that the current difference in means arises just by chance (again assuming independent measurements), is 1.7×10^{-15}.

A summary of the average spatial offset (LF–HF) from the linear regression for each RTM is given in Figure 8. The migrations in Figure 7, chosen because they occupy essentially the same portion of the fault but with nearly opposing propagation directions, are illustrated in Figure 8a. Each offset is denoted by a circle indicating the mean value (difference in intercepts between the LF and HF detections), bounded by the error estimate representing the 95% confidence interval from the residual distribution of the regression to the LF detections. The number of detections in both the HF and LF passbands (HF; LF) are given on the right, with more detections providing more constraints to the regression. As can be seen, the average offsets of most individual migrations in the same group (ENE or WSW) have the same sign as the mean offset of the combined detections.

Because both the confidence interval and Student's t-test assume the underlying measurements to be independent random variables, we next apply the same analysis to catalogs that include only non-overlapping windows. Although we only include temporally overlapping windows in each of our HF or LF catalogs if the two windows don't share the same strongest arrival, these catalogs nonetheless include some detections from windows that are half-overlapping. Using only the LF detections from non-overlapping windows, the corresponding distributions of the WSW- and ENE-propagating groups and the difference in the mean LF–HF offsets between the two groups are shown in Figure S17 in Supporting Information S1. It reveals that

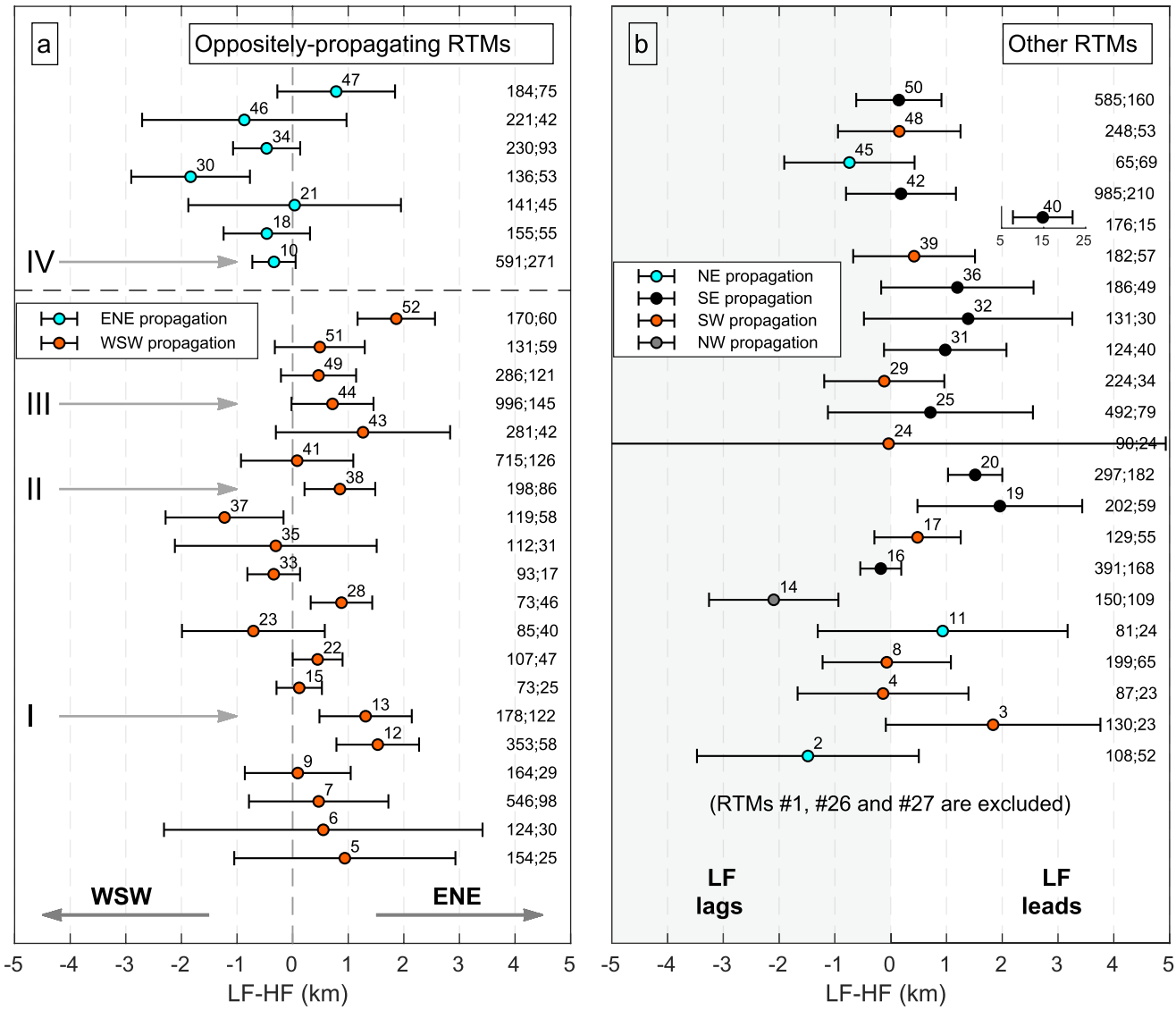

Figure 8. Summary of the average spatial offset (LF–HF) from the linear regression to each RTM identified using the TWKB trio. (a) includes the chosen migrations with nearly opposite propagation directions contributing to the histograms in Figure 7. Each offset is denoted by a circle indicating the difference in intercepts between the LF and HF detections as obtained in Figure 6c, bounded by the error estimate representing the 95% confidence interval from the residual distribution of the LF regression. Migrations are filled in different colors by their propagation directions. The number of detections in both the HF and LF passbands (HF; LF) are given on the right. (b) summarizes the other RTMs. We exclude RTMs #1, #26 and #27 from consideration as we focus on the region of the fault hosting the nearly opposing migrations in (a). Since SE-propagating and NW-propagating RTMs also exist, the sign of the offset is set to be negative if on average the LF detections lag the HF detections in the propagation direction. Note that migration #40 has an unrealistic mean offset of 15 km and an error of ±7 km, which results from the scattered LF detections. Migration #24 has an extreme error of ±5 km for the same reason. The migration marked I is shown in Figure 6 and migrations II, III, IV are shown in Figures C1–C3 in Appendix C.

using independent detections changes the difference in means only slightly, from about 920 m in Figure 7b to 970 m in Figure S17b in Supporting Information S1. Though the width of each confidence interval increases due to the smaller sample size, the two confidence intervals are still well separated. In terms of the significance of the difference, the p-value from the t-test is 1.8×10^{-10}.

The largest source of inter-dependence of our LF–HF measurements likely comes from the choice of propagation direction. For example, choosing two directions that differ by 180° flips the sign of every leading or lagging measurement for that migration. One could imagine that choosing the maximum-speed direction over the minimum-RMSE direction (determined from the HF detections) as the propagation direction for five migrations (e.g., Figure C4) could influence the separation of the confidence intervals in

Figure 7b. To test this possibility, we re-select the nearly-oppositely-propagating RTMs after adopting the minimum-RMSE direction (determined from the HF detections) as the propagation direction for all 52 migrations. This results in five migrations in the ENE-propagating group and 18 in the WSW-propagating group, and increases the separation of the 99% confidence intervals by ∼300 m (Figure S18 in Supporting Information S1). We also note from Figure 7b and Figure S17b in Supporting Information S1 that LF sources lag the HF sources for both the ENE- and WSW-propagating RTMs by ∼500 m. Therefore, the aforementioned 1-km threshold for the absolute difference in offset we use to decide which migrations should be considered separately may be too high. In Figure S19 in Supporting Information S1 we show histograms that use only opposing migrations for which the absolute difference in the spatial offset LF–HF between the minimum-RMSE and maximum-speed directions is smaller than 500 m (Figure S20 in Supporting Information S1). This set includes 5 migrations in the ENE-propagating group and 11 in the WSW-propagating group, and decreases the separation of two means by ∼200 m, but the 99% confidence intervals of the means remain separated.

A second source of inter-dependence of our LF–HF measurements comes from treating migrations that are not strictly linear as linear. Here we hope that our statistics are robust, and that this inter-dependence is averaged out, by including all the migrations available to us that have a range of acceptable qualities.

The inset to Figure 4 shows that although the ENE-WSW component of the filtering effect corrections are largely consistent across the region of opposing ENE-WSW migrations, families 017, 043, 068, and 099 differ from the "consensus" of ∼400–600 m by roughly ±500 m. This is a significant fraction of the difference between the mean LF–HF offsets of the WSW- and ENE-propagating groups. If any of these corrections is spurious, and the associated LFE family contributes many more detections to either the ENE- or WSW-propagating migrations than to the other, it could potentially bias the difference in mean LF–HF offsets between the two groups. We find that this is not the case. First, plots of the proportion of detections in every migration tied to a particular LFE family (one plot for each family) show that there is no LFE family that contributes much more to one of the ENE- or WSW-propagating groups than the other (Figure S21 in Supporting Information S1). Second, plots of the average spatial offset (LF–HF) of every migration vs. the proportion of detections in that migration tied to a particular LFE family (one plot for each family) show no strong correlation, except for family 068 (Figure S22 in Supporting Information S1). However, roughly the same positive correlation applies to both the ENE- and WSW-propagating groups for this family, which means that the mean LF–HF offsets from both groups would increase as the proportion increases, but the difference in offsets between the two groups would persist. Finally, we re-run our detection and location procedure while eliminating (one at a time) each of the possibly anomalous LFE families 017, 043, 068 and 099. This reduces the number of detections in each migration only slightly, because detections seen by one family are often seen by at least one other. We find that the mean LF–HF offsets are essentially unaffected by this procedure (Figures S23–S26 in Supporting Information S1).

6. Discussion

We have shown that LF detections seem to consistently locate differently from HF detections, relative to the propagating fronts of RTMs, but whether LF detections lag or lead HF detections needs more discussion. In Figure 7b (as well as Figures S17–S19, S23–26 and S28 in Supporting Information S1), LF detections seem to lag HF detections on average by anywhere from 350 to 700 m. Thus a 500-m error in the ENE component of the filtering effect correction would imply that for RTMs propagating in one direction the LF sources would be roughly coincident with the HF sources, while for those propagating in the other they would lag by ∼1 km. A 1-km error would imply that the LF sources would lead the HF by roughly 0.5 km in one propagation direction, but lag by 1.5 km in the other. It seems hard to rationalize such behavior, and given the magnitudes and consistency of the filtering effect corrections among the different families in the inset to Figure 4, we prefer the interpretation that the LF sources lag the HF sources in the propagation direction for both the ENE- and WSW-propagating RTMs by ∼500 m. This would require an error in the filtering effect corrections of ∼100 m, or about 20% of the correction in the ENE-WSW direction, which seems reasonable given the consistency of the corrections in Figure 4. However, we note

that the individual migrations in the two groups differ in spatial extent, duration, number of detections, propagation (and perhaps slip) velocity, etc., so the mean offsets of the two groups are not necessarily the same. But for modest errors in the filtering effect corrections the LF signals would always lag the HF signals in both propagation directions.

We recognize that what we call the opposing migrations do not propagate in strictly opposite directions, as the "ENE-propagating" group is on average more nearly E-propagating, so any errors in the filtering effect corrections may not affect the two groups equally. In Appendix D we assess in detail the implications of this for the uncertainty in our estimated LF–HF offset for the two groups. We first estimate an upper bound on the uncertainty in the filtering effect corrections due to random cross-correlation errors, based on the scatter in the measured filtering effect corrections for the 9 LFE families in the NW portion of our study area (Figure D1a). The relevant errors in the filtering effect corrections are those that are roughly aligned with the measured corrections, since that direction more-or-less bisects the E- and WSW-propagating directions. Thus, errors in this direction move the histograms of the two groups in Figure 7 toward or away from one another by comparable amounts. The scatter of the 9 filtering effect corrections in this direction is ∼±1 km, which, given that the two migration groups are nearly opposing, is sufficient to change the LF–HF offsets by only ∼1/5 of that distance, from −500 m to ∼−300 m for true corrections that are 1 km larger than our measured corrections. Larger systematic errors in the filtering effect corrections, such that the true values were 2.5 km larger that our measured values, could reduce the LF–HF offset from −500 m to ∼0 for both groups (red dots in Figures D1b and D1d). However, regardless of how plausible such large systematic errors are, information from the migrations not belonging to the nearly opposing groups suggest that this scenario is unlikely.

Figure 8b shows the average spatial offset (LF–HF) for the other RTMs, using the measured filtering effect corrections. We exclude migrations #1, #26 and #27 (dashed black arrows in Figure D2a) from consideration, as they occupy a different region of the fault from the nearly-opposing migrations in Figure 8a, and the assumption of reasonably similar filtering effect corrections seems less reliable. The discarded migrations contain 166 LF detections, amounting to ∼10% of those not belonging to the two nearly-opposing groups. Most of the LF detections within the remaining migrations are attached to migrations that propagate within a fairly narrow range of azimuths to the SE (Figure D2a). To analyze these migrations, we set the sign of the LF–HF offset to be negative if on average the LF detections lag the HF detections in the RTM propagation direction. Generating a histogram for this set (Figure D2b), as was done in Figure 7b, indicates that on average the LF detections lead the HF detections by about 390 m (or 280 m if we did not discard those three migrations). Because these LF–HF offsets are dominated by migrations moving to the SE, close to the orientation of the measured filtering effect, changing the filtering effect corrections in that direction changes the LF–HF offsets for this group by a roughly comparable amount. Thus, for example, the filtering effect mentioned above that is 2.5 km larger, and that reduces the LF–HF offsets to nearly zero for both opposing groups in Figures 7 and 8a, increases the LF–HF offset for the migrations in Figure 8b from 390 m to 2.1 km (LF leads HF). This conflicts with the simplest a priori expectation, that the LF–HF offsets in the reference frame of the migrating front should be independent of migration direction. In Appendix D we search for filtering effect corrections that minimize the difference between the LF–HF offsets for the three groups (the E-propagating and WSW-propagating groups in Figure 8a, and the remaining migrations in Figure 8b), while simultaneously minimizing the difference from our measured filtering effect. We find that a correction that is roughly 1.3 km less than, and in the same direction as, the measured corrections, changes the average offset for the migrations in Figure 8b by ∼−800 m, from +390 m to ∼−410 m, and those for the E-propagating and WSW-propagating migrations in Figure 8a by ∼−200 m, from ∼−500 m to ∼−700 m. While we have no quantitative mechanism for estimating how large a systematic error in the filtering effect corrections is plausible, an error of 1.3 km is not much larger than our upper-bound estimate of random cross-correlation errors, and is only about 15%–20% of the filtering effect corrections determined via cross-correlation of the LFE templates.

If one accepts that lower-frequency tremor signals lag the higher-frequency signals in the propagation direction of RTMs, the simplest interpretation is that the seismic signal emanating from regions closer to the propagating slip front is enriched in high frequencies relative to regions farther behind. In a Barenblatt cohesive zone crack model (Barenblatt, 1962), slip speeds rapidly reach a maximum close

to the rupture front and decay more slowly behind. Thus any process in which the frequency of velocity fluctuations increases with slip speed could account for a decrease in source frequency behind the rupture front.

The main goal of this research has been to investigate the source of the coherent LF signals in tremor. We hypothesize that if the lower-frequency signals come from the overlapping of higher-frequency LFEs that are randomly distributed in time, then the LF and HF signals would be nearly co-located. Alternatively, if the lower-frequency signals are generated from longer-period sources other than higher-frequency LFEs, this could manifest as a spatial offset between the two. The statistical tests described above support the consistent difference in average spatial location between contemporaneous LF and HF detections (LF–LF) during rapid tremor migrations. This seems unlikely to arise from higher-frequency LFEs that are distributed randomly in time and space, in the moving reference frame of a propagating RTM front. However, it remains to be established whether some non-uniform distribution of higher-frequency LFEs behind the RTM front could give rise to an apparent offset between contemporaneous HF and LF sources (for example, stronger but more temporally isolated higher-frequency LFEs near the front, simultaneously with temporally-overlapping but weaker LFEs farther behind the front). This possibility could be explored with synthetic seismograms made up of non-uniformly distributed LFE templates in future work. Barring this possibility, our results suggest that the LF (0.5–1.25 Hz) signals have a source which is indeed distinct from just the temporal overlapping of typical higher-frequency (1.25–6.5 Hz) LFEs. One possibility is that the frequency of seismic radiation produced at a given location is not fixed by time-invariant fault-zone properties, but that the same location is capable of producing signals of varying frequency, depending (e.g.,) upon the current average or background slip speed. This feature, that the characteristics of seismic radiation from a particular location on the fault depend on more than just the spatial distribution of fault properties, is also a property of the broadband stochastic model of Ide (2008, 2010), although he did not explicitly consider the spatial relationship between sources of different frequency. An alternative is that spatially distinct LF and HF sources are interspersed on the subduction interface. Given the strongly overlapping distribution of LF and HF sources in Figure 5, this would require mixing of these discrete regions on a finer scale than our location error, and on average the LF sources would have to be triggered farther behind the propagating RTM front (requiring greater total slip, perhaps).

7. Conclusions

In this paper we detect and locate tremor signals beneath southern Vancouver Island separately in relatively high-frequency (1.25–6.5 Hz; HF) and low-frequency (0.5–1.25 Hz; LF) bands, focusing on the three-station detector TWKB-LZB-MGCB. We hypothesize that if tremor consists entirely of LFEs, so that the lower-frequency signal in tremor comes just from the non-uniform timing of higher-frequency (~2 Hz) LFEs, contemporaneous LF and HF signals would be nearly co-located. Alternatively, if the LF signals have a source distinct from overlapping higher-frequency LFEs, a spatial offset between the two sources might be present. Overall, we find some subtle differences in source locations between the HF and LF catalogs (Figure 5). However, owing to uncertainty in our empirical filtering effect corrections (differences in relative arrival times obtained by cross-correlation that arise just because of the different passbands applied), and to possible spatial variability in the coherence of HF and LF seismograms between the various stations (due to either source-station path effects or to spatial variability in the typical spatial extent of source regions active at one time), we think it is premature to interpret these differences in terms of different fixed locations for HF and LF sources.

Instead, we identify 27 rapid tremor migrations in the northwestern portion of our study region that propagate in nearly opposite directions (20 to the WSW and 7 to the ENE), and examine the locations of LF and HF sources relative to the propagating front. Focusing on oppositely-propagating migrations greatly reduces the influence of any errors in our filtering effect corrections. The ENE-WSW trend also has the smallest location errors and filtering effect corrections (this is not due to chance alone–the oppositely-propagating RTMs migrate mostly along the main slow slip front, which is oriented roughly parallel to the dip direction of the subduction zone, as was the POLARIS array). We find that LF detections consistently lag HF detections, by about 500–700 m for migrations propagating to the WSW and about 300–400 m for migrations

propagating to the ENE. Although this LF–HF offset is smaller than the location errors of our LF catalog, given the more than 1,000 LF detections the result appears to be robust. Our preferred interpretation is that the LF sources lag the HF sources in both propagation directions by roughly the same amount (~500 m), which would require a ~100-m error in the ENE-WSW component of our filtering effect correction. This LF–HF offset is robust in the presence of random cross-correlation errors in the filtering effect corrections. In contrast, the average LF–HF offset for the remaining 22 RTMs occupying the same portion of the fault seems inconsistent with that for the nearly-opposing RTMs. However, a systematic error that makes the true filtering effect corrections ~1.3 km smaller than and in the same direction as the corrections measured from cross-correlating the LFE templates, could make the average LF–HF offsets for all three RTM groups in this study (Figure 8) consistent with one another, at a value of ~−600 m.

This persistent spatial offset suggests that the LF (0.5–1.25 Hz) signals have a source distinct from just the temporal overlapping of typical higher-frequency (1.25–6.5 Hz) LFEs. One interpretation is that a given location on the subduction interface, rather than generating a signal of fixed frequency tied to time-invariant fault-zone properties, instead radiates seismic energy at a frequency that depends upon the loading conditions (e.g., that decreases as the local average sliding speed decreases). Such a process seems consistent with so-called LFEs and tremor being manifestations of the same broadband stochastic process, as suggested by Ide (2008, 2010). Alternatively, relatively high-frequency and low-frequency sources can be mixed in the fault zone at a scale finer than our spatial resolution, with the lower-frequency sources being triggered farther behind the propagating front of tremor migrations.

Appendix A: Shear-Wave Splitting Corrections

As demonstrated by Bostock and Christensen (2012), there is significant crustal anisotropy beneath southern Vancouver Island, resulting in spatially-varying shear-wave splitting and polarization. Using a method similar to that of Peng et al. (2015), we empirically calculate the split times and fast polarization directions for each LFE family, and assume that these are representative of the splitting parameters in the surrounding region. These splitting parameters are determined via a grid search to maximize the cross-correlation (CC) coefficient between the fast and slow components of the LFE templates. For every LFE family at each station, we first obtain a preliminary stack of the broadband N and E component seismograms using time windows determined from the LFE catalog of Bostock et al. (2012). To maintain consistency with our detection/location method, we then filter these broadband stacks from 0.5–6.5 Hz. Next, we rotate and cross-correlate these N and E templates from 0–175°, in 5-degree increments, to find the angle that maximizes the maximum CC coefficient at that station. We note this angle as the slow or fast direction, depending on the sign of the differential travel time between the rotated N and E templates, and the differential travel time resulting from that angle as the split time. For this cross-correlation we use only the 1.5-s segment containing the main dipole arrival to reduce interference from the *S*-wave coda. We recognize the shear splitting as significant only if the split time is at least 0.05 s.

Figure S27 in Supporting Information S1 shows the obtained split times and fast wave directions for all LFE families using the TWKB detector. The result seems reliable, in that the split times and fast wave directions for different families at the same station vary smoothly in space. Moreover, the variation of these parameters at different stations for the same family is small. Although the adopted families are not exactly the same and locations of some families have been updated, our result is consistent with that in Figure S3 of Peng et al. (2015). We correct for the shear-wave splitting by aligning the fast and slow components using the split time and rotating them back to N and E.

Next, we determine the optimal shear-wave particle motion directions. We again rotate these (now split-corrected) N and E templates from 0–175° in increments of 5°, and compute the ratio of energy (sum of the squared amplitude) between the two components and find the angle at which this ratio reaches its maximum. At this angle we refer to the direction of maximum energy as the "optimal" orientation; this is the inferred shear-wave particle motion direction. We refer to the corresponding direction of minimum energy as the "orthogonal" orientation. Following this procedure, we are able to transform the raw N and E seismograms at each station into one optimal trace for each LFE family, where the shear-wave splitting is corrected for and most of the shear energy is concentrated. For the same LFE family, we then stack the

optimal traces to obtain a preliminary template using time windows determined from the LFE catalog of Bostock et al. (2012). Because the member LFEs do not all have the same hypocenter, we refine the template by shifting each LFE by up to ±0.25 s to maximize the CC coefficient with the preliminary stack, and then re-stack those slightly time-shifted LFEs. To determine the approximate travel-time offsets between the different stations for sources located in the vicinity of each LFE family, we cross-correlate the split-corrected optimal templates at stations with that at the reference station (e.g., TWKB for the TWKB detector).

Appendix B: Tremor Detection in HF and LF Passbands

Many studies have employed a "cross-time" method to locate LFEs and tremor, meaning that the fundamental correlation measurement is between two different time windows at one station. The cross-correlation can be between the target time window and either a nearby previously-identified LFE (Shelly et al., 2007b), or a stack of many nearly co-located LFEs (e.g., Brown et al., 2009; Bostock et al., 2012; Shelly, 2010). However, this method will result in detected time windows that are highly coherent with the template. As we are wondering if there are any other signals besides the 0.5-s LFEs in tremor, prescribing any template for detection may miss longer-period signals. In contrast, a "cross-station" method, first proposed by Armbruster and Kim (2010) and further developed in Armbruster et al. (2014), Rubin and Armbruster (2013) and Peng et al. (2015), compares waveforms of the same time window (after accounting for travel-time differences) at two widely separated stations, by taking advantage of the coherence in tremor records across stations. Cross-station methods perform well when the response to an impulsive source at each contributing station is dominated by the direct *S*-wave arrival rather than its coda or any converted phases. In such cases the method effectively cross-correlates the source-time function in each time window, provided the sources are nearly co-located so that the differential travel times to the various stations are roughly constant.

As in Peng et al. (2015), we obtain trial tremor catalogs associated with each adopted LFE family by rotating the N and E component waveforms at each station to obtain a single-component seismogram, that represents our best guess for the shear-wave particle motion direction after correcting for shear-wave splitting. These directions and splitting parameters are determined for each LFE family-station pair as described in Appendix A, using the passband 0.5–6.5 Hz. Consistent with the generally small differences between nearby families, we assume that these parameters vary slowly over the fault, so that they are useful for sources located within several kilometers of the associated LFE family. The seismograms are then filtered using the passbands 1.25–6.5 Hz (HF) and 0.5–1.25 Hz (LF).

To make detections, we employ a sliding time window with a fixed length (4 s for HF; 16 s for LF) and sliding step (1 s for HF; 8 s for LF) to cross-correlate the three station pairs (Rubin & Armbruster, 2013). With the general time offsets between stations for signal coming from the vicinity of each LFE family as determined in Appendix A, we enforce a maximum possible lag around that expectation when cross-correlating the processed daily seismograms. The maximum allowed time lag is ±0.35 s for the HF catalog using the TWKB trio to the data sampled at 40 Hz.

For the HF catalog, a successful detection requires the maximum cross-correlation (CC) coefficient, averaged over the three station pairs, to be higher than 0.4, and the circuit of three time offsets between the station pairs that achieve this maximum (OFF_{max}) to be less than 0.0375 s in magnitude. Both thresholds were set by trial and error. In principle, they should be strict enough to avoid those presumed "false positives" that are spatially or temporally isolated, without reducing much the total number of clustered detections, which are likely to be real seismic sources. Given a successful detection, we interpolate the offsets to a quarter sample at 40 Hz (i.e., 0.00625 s) and then force the circuit of time offsets to be zero, and choose the two independent time offsets that maximize the average CC coefficient for the 3 station pairs (that must again be higher than 0.4).

As a third quality-control measure to help weed out false positives, we require that the ratio of energy on the optimal component to that on the orthogonal component, $R_{o/o}$, be larger than 3 at the time of the strongest "arrival" in the window (Peng et al., 2015). To identify this arrival, we first multiply the aligned seismogram pairs in each window point-wise, and average over the three pairs. For velocity seismograms

this is a proxy for the coherent radiated energy rate in the analyzed passband, and we denote it as $\dot{E}'$ (Rubin & Armbruster, 2013):

$$\dot{E}'(t) = \frac{S_1(t)S_2(t'_2) + S_1(t)S_3(t'_3) + S_2(t'_2)S_3(t'_3)}{3}, \tag{B1}$$

where the subscripts 1, 2 and 3 denote the stations TWKB, LZB and MGCB in the TWKB trio, $S(t)$ is the seismogram, and t' represents the time offset between the arrival at station 2 or 3 and station 1. The time that reaches the maximum $\dot{E}'$ is noted as the most energetic arrival of the detected window. We determine $R_{o/o}$ over a time window that extends over $\pm\delta t_{\min}$ from this most energetic arrival, via

$$R_{o/o} = \frac{\sum^{2\delta t_{\min}}(S^2_{1opt}(t) + S^2_{2opt}(t'_2) + S^2_{3opt}(t'_3))}{\sum^{2\delta t_{\min}}(S^2_{1ort}(t) + S^2_{2ort}(t'_2) + S^2_{3ort}(t'_3))}, \tag{B2}$$

where the subscripts "opt" and "ort" denote the optimal and orthogonal components, respectively. We take $\delta t_{\min}$ to be the approximate duration of the dipole in the stacked templates, 0.5 s in HF (e.g., Figure 3b).

To avoid double-counting of the same event because of the overlapping detecting windows, we do not preserve all detected windows. We accept both of two overlapping windows only if their most energetic arrivals are separated at least by $\delta t_{\min}$, otherwise we only preserve the one with a larger average CC coefficient. This may admit two sources separated more than 0.5 s, or a single source twice if it radiates longer than 0.5 s.

As the LF detections invariably have a lower location resolution due to the widening of the waveform, we down-sample the seismograms from 40 to 20 Hz. Due to a generally lower signal-to-noise ratio and a narrower passband (a factor of 2.5 between the high and low frequency limits rather than the factor of 5.2 for the HF band), the LF catalog is also more prone to cycle skipping. To guard against the possibility that LF sources lie outside our maximum allowable time lag but, via a cycle skip, have a secondary CC maximum that places them within our region of interest, we increase the time lag over which we search for the maximum CC value to ±1.7 s, but retain in the catalog only those detections with lags up to ±0.7 s. The difference of 1 s is approximately the expectation for a single cycle skip. For 16-s windows, threshold values of $CC_{\min} = 0.35$ and $OFF_{\max} = \pm 0.2$ s were deemed suitable. As the width of the dipole-like arrival is larger at lower frequencies (e.g., Figure 3c), $\delta t_{\min}$ is set to be 1.1 s. For the LF catalog, $R_{o/o}$ must exceed 1.5.

Because the splitting parameters and dominant particle motion directions appear to vary smoothly in space, HF detections up to 8 km and LF detections up to 12 km from their parent LFE family are permitted. Adopting this criterion, some detections are common to 2 or more LFE families. The final HF and LF catalogs are made by merging the detections tied to each LFE family. In the event that a detected window is common to more than one family (meaning more than one set of splitting and rotation parameters), we choose the one that gave rise to the largest CC value. As station TWKB is the reference station for all LFE families, the time limits of all windows for the catalogs tied to all LFE families are identical at TWKB, which makes identifying duplicate detections straightforward. The catalog that results from merging those based on all the 13 LFE families using the TWKB detector contains 51,057 HF detections and 18,491 LF detections (23 days, 1–5 March 2003, 12–21 July 2004 and 11–18 September 2005).

Appendix C: More RTM Examples

In the main text, we showed one migration detected using the TWKB trio to demonstrate the regression analysis. Here we show 2 more examples (Figures C1 and C2) from the WSW-propagating group and 1 example (Figure C3) from the ENE-propagating group, that are labeled in Figure 8a. We also show one migration (Figure C4) from the ENE-propagating group in Figure 8a where we choose the maximum-speed direction (in HF) as the propagation direction, rather than the default minimum-RMSE direction. All the other oppositely-propagating migrations included in Figure 8a are shown in Figures S29–S49 in Supporting Information S1.

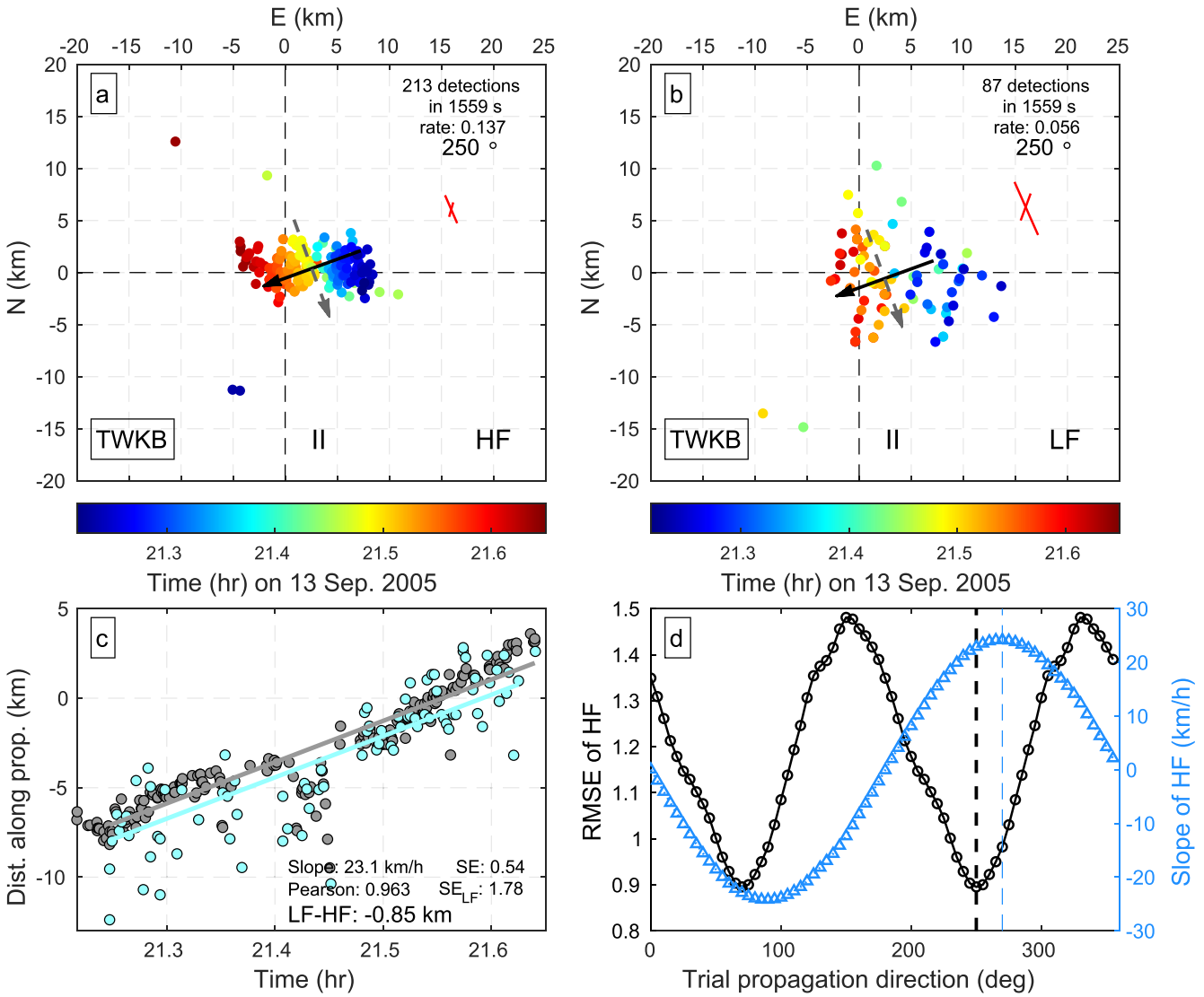

Figure C1. One RTM occurring from 21.2 to 21.7 h on September 13, 2005 from the WSW-propagating group detected using the TWKB trio. Symbols are the same as in Figure 6.

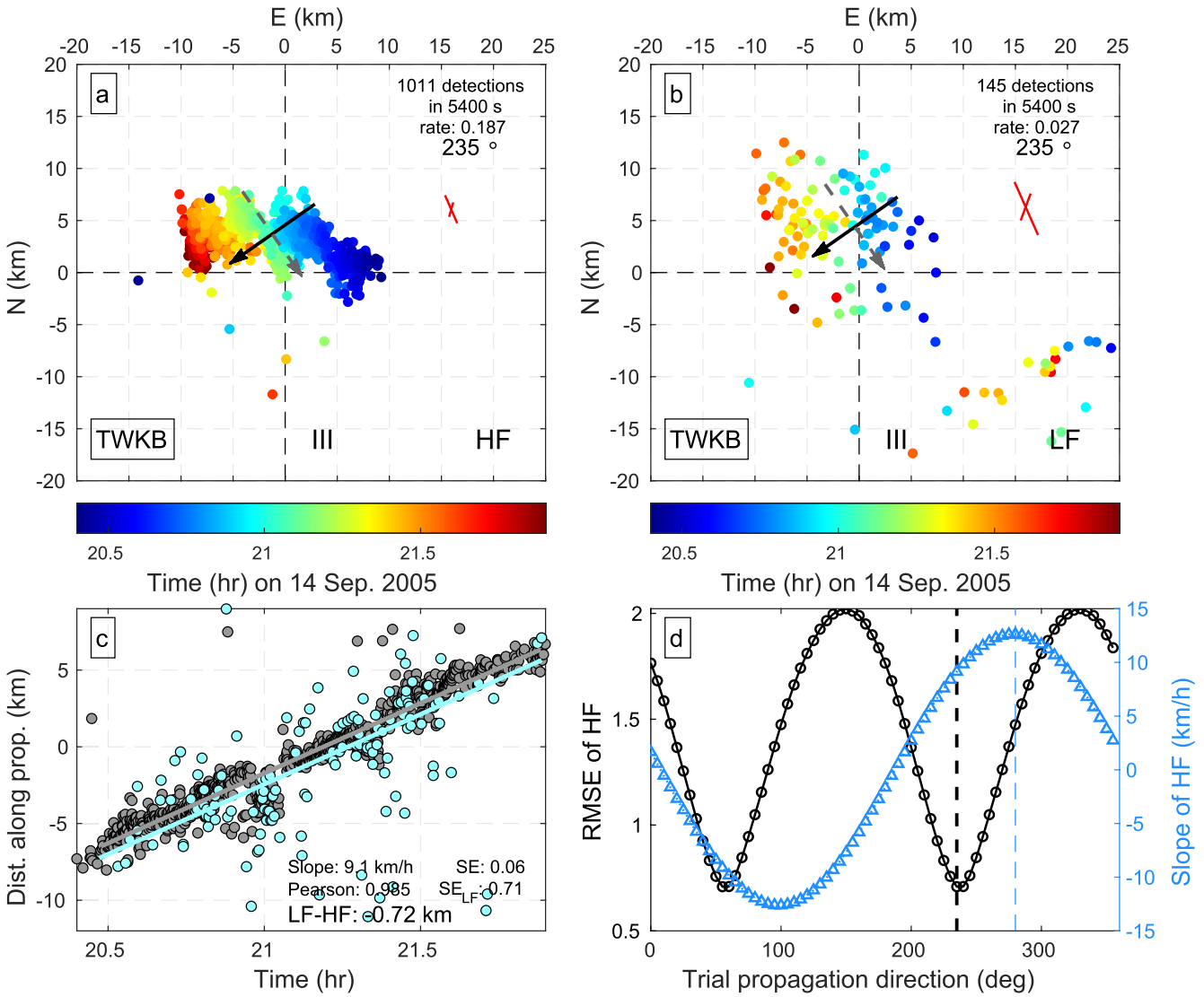

Figure C2. One RTM occurring from 20.4 to 22 h on September 14, 2005 from the WSW-propagating group detected using the TWKB trio. Symbols are the same as in Figure 6.

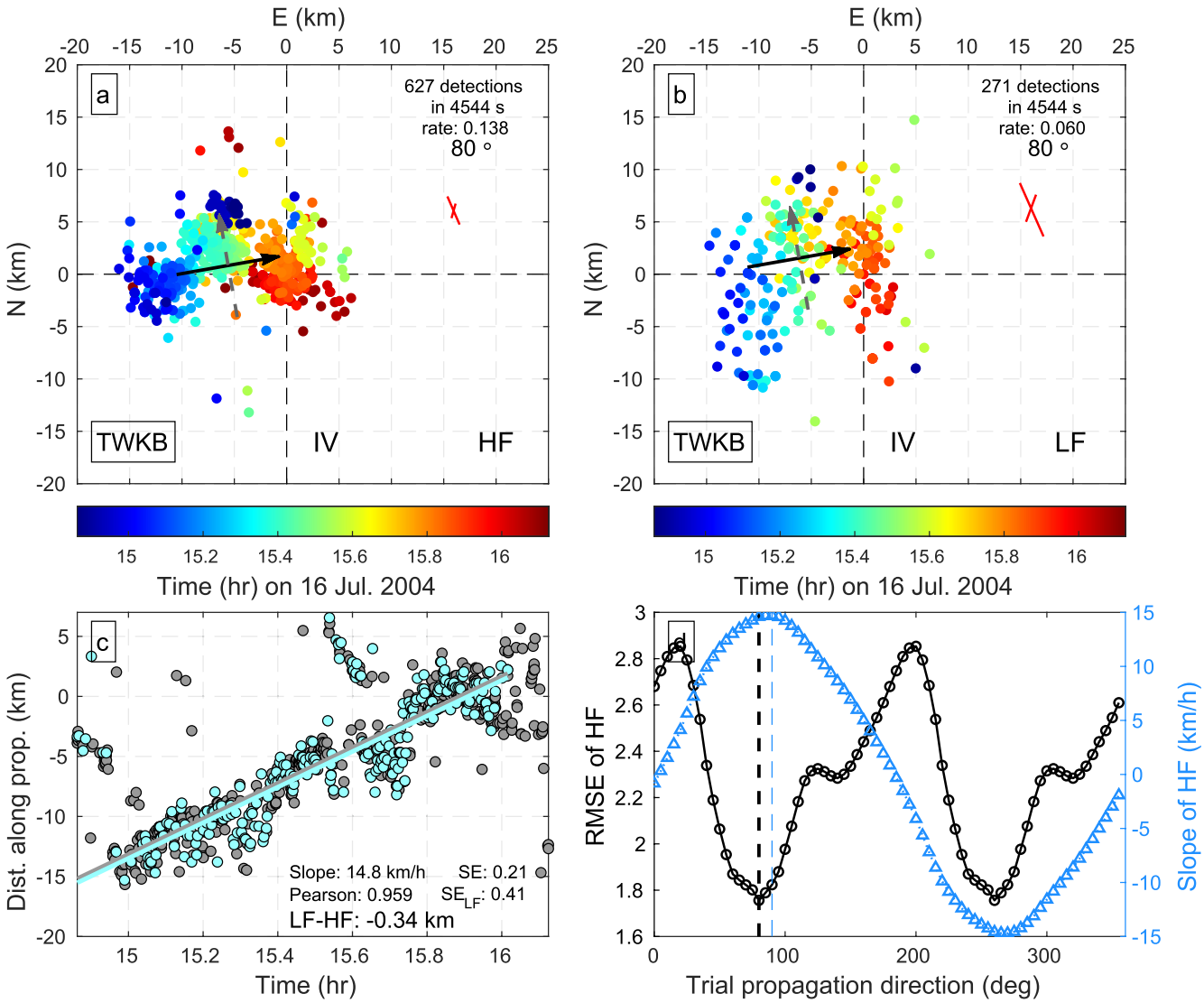

Figure C3. One RTM occurring from 14.9 to 16.1 h on July 16, 2004 from the ENE-propagating group detected using the TWKB trio. Symbols are the same as in Figure 6.

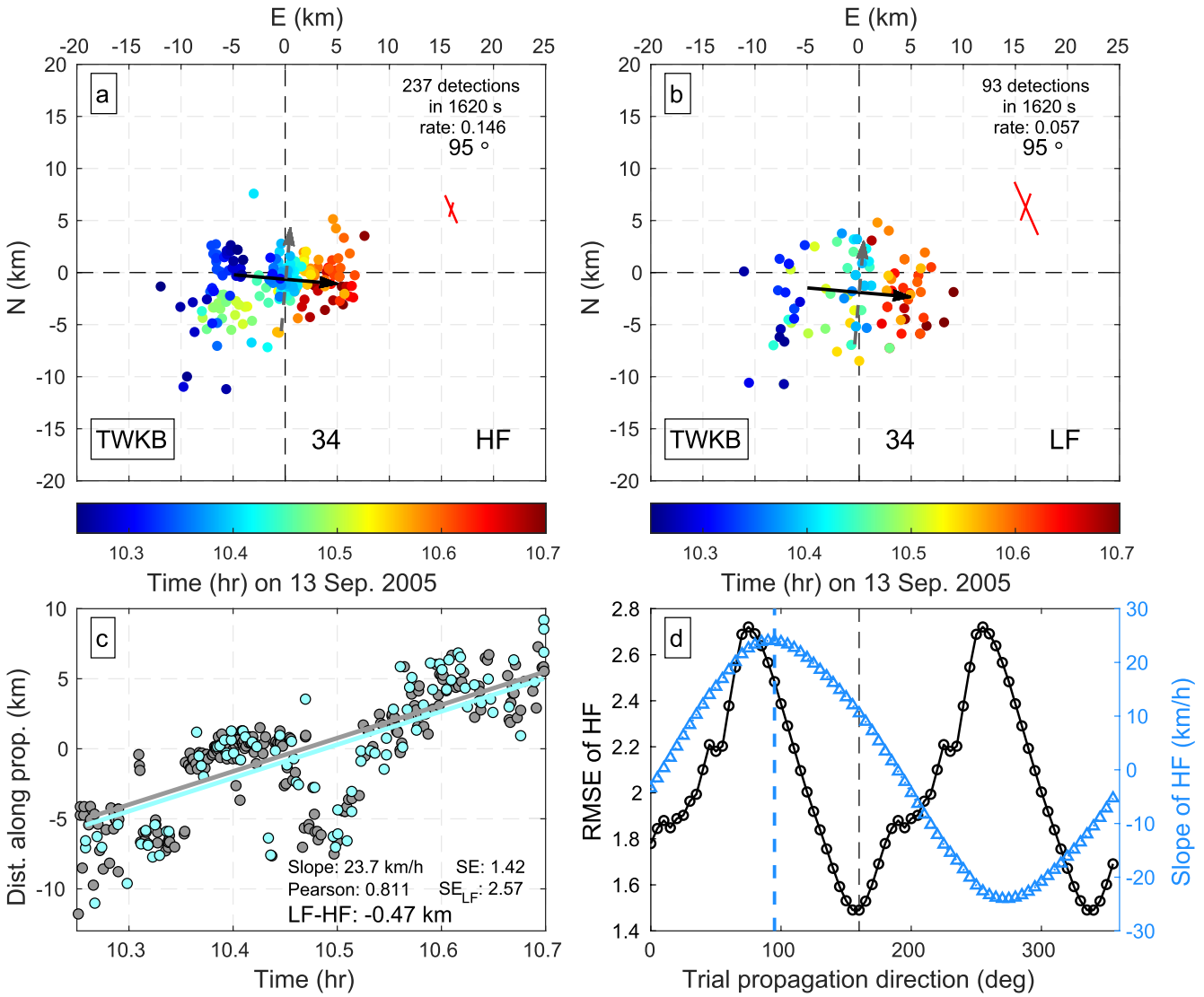

Figure C4. One RTM occurring from 10.3 to 10.7 h on September 13, 2005 from the ENE-propagating group detected using the TWKB trio. For this RTM we use the maximum-speed direction as the propagation direction, because the Pearson correlation of the fit to HF detections using this direction is higher by 0.15 than that using the default minimum-RMSE direction, which is nearly N–S, and the maximum-speed direction also is visually better. Symbols are the same as in Figure 6.

In Figure S16 in Supporting Information S1 we plot cumulative density maps of the HF and LF detections belonging to the migrations of the ENE-propagating and WSW-propagating groups in Figure 8a. These maps show that to a large extent the migrations of the ENE- and WSW-propagating groups occupy the same portion of the fault. In Figures S16b and S16d in Supporting Information S1, a few tens of LF detections from the WSW-propagating group are located in the vicinity of LFE family 002. LF detections in this area are nearly absent from the ENE-propagating group. These detections are from migrations (e.g., migration III in Figure C2) whose majority lie in the northwestern portion of the study region. Excluding the spatial offset (LF–HF) measurements tied to those LF detections from the histograms in Figure 7b does not substantially alter the mean offsets and their difference (see Figure S28 in Supporting Information S1) because the number of LF detections in this vicinity is very small compared to the majority.

Appendix D: Quantifying the Influence of Possible Errors in the Filtering Effect Corrections

The two groups of migrations in Figures 7 and 8a do not propagate in exactly opposite directions, so any errors in the filtering effect corrections do not affect the two groups equally. Here we attempt to quantify the implications of this. In the process, we are also able to make use of the migrations in Figure 8b, those that do not consist of opposing pairs.

The first step is to assess the magnitude of possible errors in the adopted filtering effect corrections. Figure D1a provides one such estimate, based on the scatter of the filtering effect corrections themselves, for the 9 LFE families of primary interest (those contributing to the inset to Figure 4). We move the SE end of the relevant 9 gray bars in Figure 4 to a common origin at [0,0]. Given a sufficiently large number of samples (here we have 9), the size of the convex boundary containing the corrections (shown here as black dots) defines roughly the upper bound of the uncertainty in the filtering effect corrections due to random cross-correlation errors. This is an upper bound to the random measurement error, given enough samples, because it supposes that the actual filtering effects for all these families are identical, whereas we have no reason to believe that this is the case; in addition, because we use several families with independently-determined filtering effect corrections, presumably the random errors cancel out to some extent.

We note that the polygon in Figure D1a has roughly the aspect ratio and orientation of the red cross in Figure 4. Therefore in Figure D1b we produce a more complete "error ellipse" by choosing 4,573 Gaussian-distributed random time offsets of up to ±0.05 s (±2 samples at 40 Hz) in Δt_{12} and Δt_{13}, with a standard deviation of 0.025 s. These time-offset pairs are treated as random cross-correlation errors and converted to locations (black dots within the black polygon) relative to the adopted filtering effect correction of family 043 (gray line), which we use here as a reference (the number of dots visible in Figure D1b is less than 4,573 because of the limited spatial resolution of our implementation of Hypoinverse). The encompassing black polygon has roughly the same shape and orientation of the polygon encompassing the filtering effect corrections in Figure D1a, considering the rather modest number of the latter, consistent with the hypothesis that the spread of the filtering effect corrections is dominated by random cross-correlation errors. The long axis of the polygon in Figure D1b (~6.5 km) is roughly 3 times that in Figure D1a (~2.25 km), suggesting that the cross-correlation error of ±0.05 s adopted for illustration purposes is a factor of nearly 3 too high (recall that the filtering effect correction is derived from the stacked templates, which have a much higher signal-to-noise ratio than the individual LF detections). Shrinking the polygon by the factor of 3, the estimated cross-correlation errors in the two median orientations of our E-propagating and WSW-propagating RTM groups (blue arrows) are roughly ±350 m. However, because these migration directions are close to 180° apart, these errors are strongly correlated; if they were precisely 180° apart, any error in the filtering effect correction would shift the histograms in Figure 7b by the same amount, preserving their separation.

We next estimate how these various potential errors in the filtering effect corrections affect the LF–HF offset relative to the migrating front. We illustrate this first for the migrations in Figure 8b, those that were left out of Figure 7 because they traversed the same region of the fault but did not belong to oppositely-propagating groups (Figure D2a). In Figure D2b we have generated a single histogram of LF–HF offsets relative to the migrating front for these migrations (gray arrows in Figure D2a), using our measured filtering effect corrections. If this represents the true filtering effect, then our estimated lag between HF and LF detections in the reference frame of the migrating front are on average correct, subject only to random measurement errors of the individual detections. We then treat each black dot in Figure D1b as the true filtering effect correction, and adjust the LF–HF measurements for each migration by the amount of the difference between the true (black dot) and previously-adopted (NNW end of the gray bar) filtering effect correction, after projection along the propagation direction of that migration. In doing this, we are effectively assuming that the difference between the true and the measured filtering effect corrections for each of the 9 LFE families are similar (if the measured filtering effect corrections all had the same azimuth, then identical errors in the filtering effect corrections would change every LF–HF measurement for any given migration by the same amount). The adjusted LF–HF measurements from all migrations result in a new mean LF–HF offset of the histogram for each black dot. In Figure D1c we plot in gray the histogram of these mean LF–HF offsets, relative to the migrating front, for all potential filtering effect corrections in Figure D1b. Directly fitting a Gaussian to the

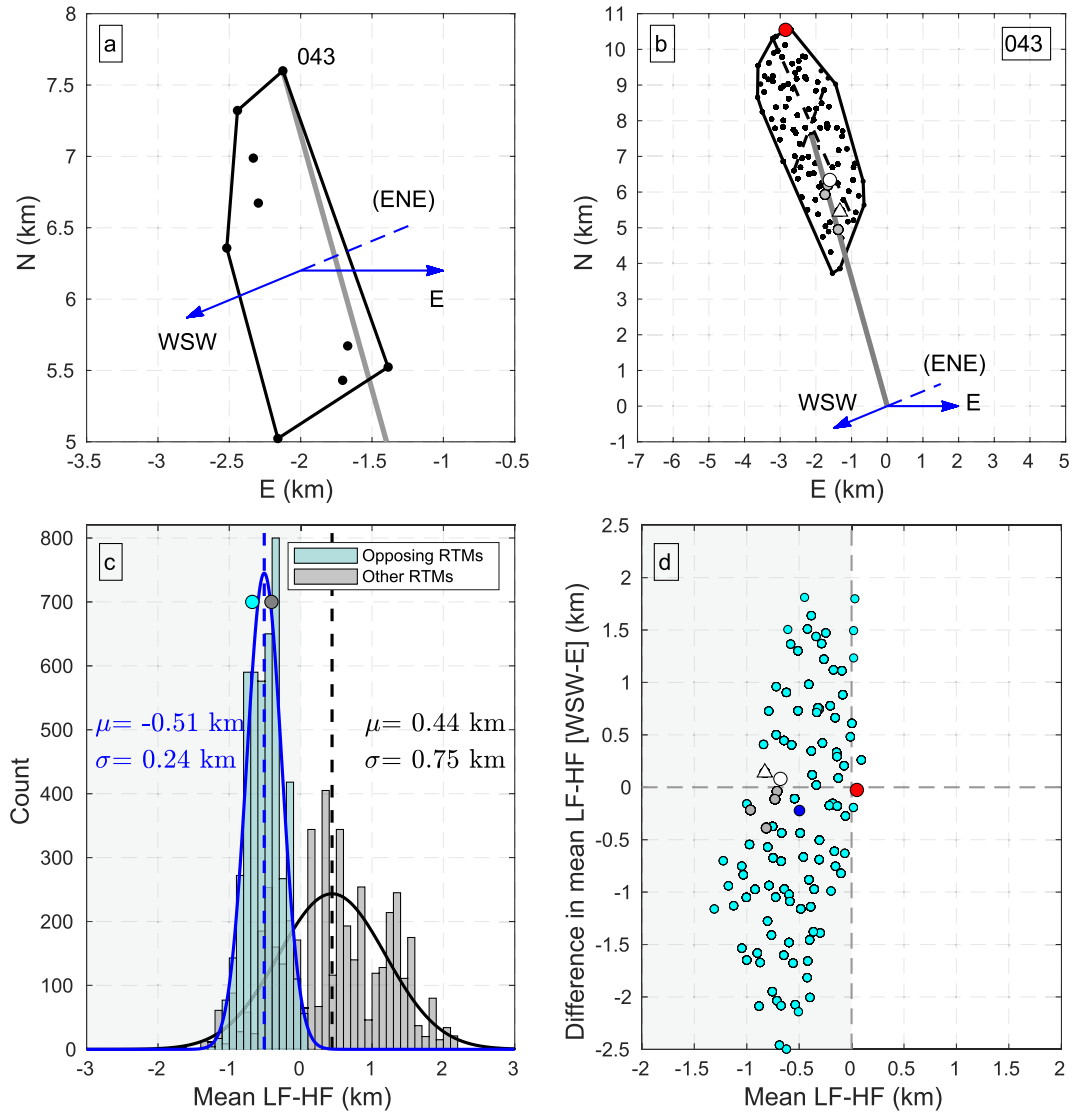

Figure D1. (a) Scatter of the filtering effect corrections (black dots) for the 9 LFE families of primary interest, made by moving the SE end of their 9 gray bars in Figure 4 to a common origin at [0,0]. The black polygon defines the convex boundary containing the corrections. The blue arrows show roughly the median orientations of our E- and WSW-propagating RTM groups. (b) Scatter resulting from 4,573 Gaussian-distributed random time offsets of up to ±0.05 s in Δt_{12} and Δt_{13}, with a standard deviation of 0.025 s. The time offset pairs are treated as cross-correlation errors and converted to locations (black dots) relative to the adopted filtering effect correction of family 043 (gray lines in both [a] and [b]). (c) shows the histograms of the mean LF–HF offset relative to the migrating front for all potential filtering effect corrections in (b), for the combined nearly-opposing RTMs in Figure 8a (cyan), and for the other RTMs in Figure 8b (gray). Negative values mean LF lags HF. The horizontal locations of the cyan and gray dots denote the mean LF–HF offsets for these two RTM groups that result from the open dot in (b), which for a modest systematic error in the filtering effect corrections makes the mean LF–HF offset for all three RTM groups reasonably consistent (see text for discussion). The open triangle in (b) leads to the most similar mean LF–HF offsets but requires a much larger systematic error in the filtering effect corrections than the open dot. Other gray dots in (b) denote the corrections for which the maximum difference between the LF–HF offsets for the three groups is smaller than 400 m. (d) is the scatter (cyan dots) of the difference in the mean LF–HF offset, relative to the migrating front, between the two nearly-opposing RTM groups (vertical axis), plotted vs. the mean LF–HF offset obtained when treating both groups as one (horizontal axis, as in [c]) for all potential filtering effect corrections in (b). The dark blue dot comes from the correction determined from cross-correlation and used in the main text. The red dot is the closest to [0,0], and the corresponding correction is denoted as the red dot in (b). The open dot, open triangle and grays dots correspond to the same symbols in (b).

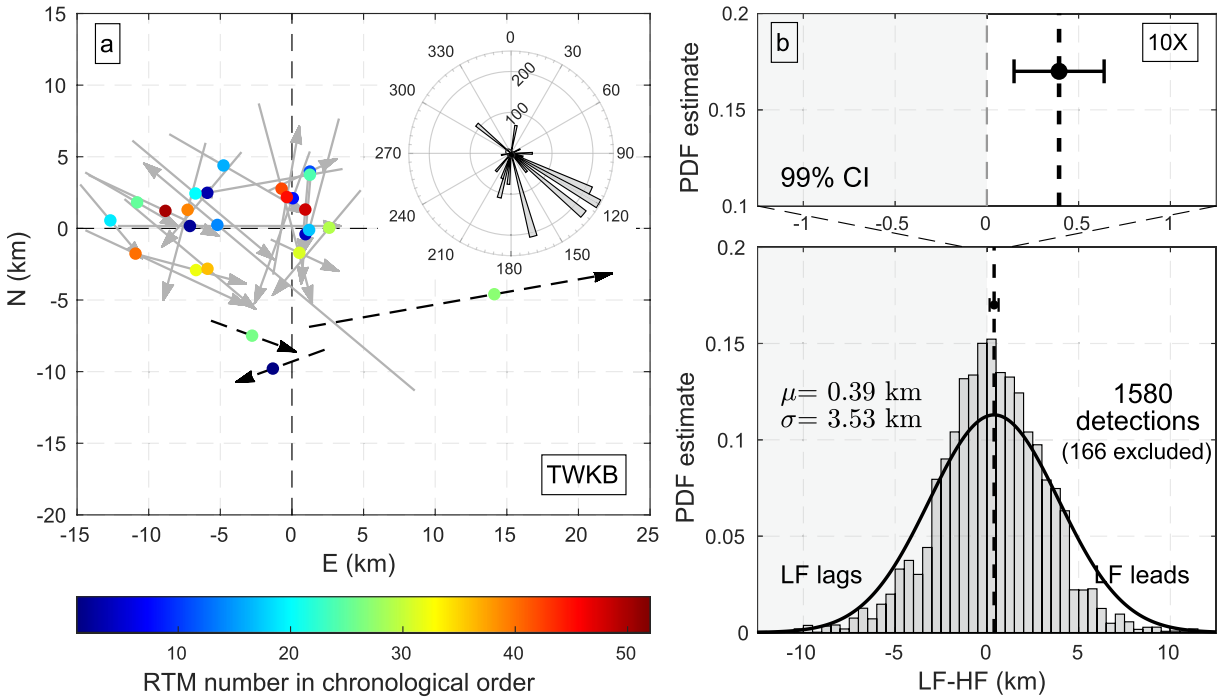

Figure D2. Histogram of the spatial offset (LF–HF) measurements from the LF detections of the other RTMs in Figure 8b. (a) shows the propagation direction and extent of these migrations. Symbols are the same as in Figure 7a. The dashed black arrows denote the three RTMs #1, #26 and #27 that we exclude because they occupy a different region of the fault. The top right inset plots the azimuths of the remaining migrations, weighted according to their number of LF detections. The lower panel of (b) plots the histogram of the LF–HF offsets. The vertical dashed line represents the (bisquare-weighted) sample mean of the offsets, which is about 390 m. The error bar centered at the sample mean is the 99% confidence interval of the mean. The upper panel of (b) shows a zoom of the confidence interval.

resulting distribution gives a μ (mean) of ~440 m and a σ (standard deviation) of ~750 m (recall that positive values of the mean imply that LF leads HF, in the reference frame of the migrating front). Reducing the spread by a factor of 3 to make the amplitudes consistent with Figure D1a leaves μ unchanged but reduces σ to ~250 m. This means that there is only a very small chance that the mean LF–HF offset would be shifted to ~ −500 m in the reference frame of the migrating front, so as to be consistent with Figure 8b, as a result of only random errors in the filtering effect corrections.

In a similar fashion, we obtain a histogram of the mean LF–HF offset for all potential filtering effect corrections for the nearly-opposing migrations in Figure 8a (cyan bars in Figure D1c). As with the gray histogram, here we treat both groups in Figure 8a as one, and plot the mean LF–HF offset relative to the migrating front. The Gaussian fitting gives a μ of ~−510 m and a σ of ~240 m. The scaled σ reduced by a factor of 3 is only ~80 m. This indicates that the mean LF–HF offset would be essentially always negative regardless of any plausible errors in the filtering effect corrections due to random cross-correlation errors.

To show the utility of having the two nearly-opposing migrations, we next separate them into their two groups, and obtain the difference in the mean LF–HF offset relative to the migrating front between the WSW- and E-propagating groups, for each of the potential filtering effect corrections in Figure D1b. The difference in the mean LF–HF offset between the two groups is shown in Figure D1d, as a function of the mean LF–HF offset obtained when treating both groups as one. The red dot in that figure is the closest to the origin [0,0], for which both the mean LF–HF offset of the combined groups (horizontal axis) and the difference in the mean LF–HF offset between two groups (vertical axis) are nearly zero. In other words, for this particular error in the filtering effect correction, for both groups there would be no location difference between the LF and HF detections on average, in the reference frame of the migrating front. The

corresponding filtering effect correction is shown as the red dot in Figure D1b; not surprisingly, it is at the edge of the distribution.

The red dot is also in the direction of the measured filtering effect correction (gray bar in Figure D1b), because that is the direction that roughly bisects the median propagation direction of the two groups. That is, any error along this direction produces an opposite effect on the LF–HF measurement for the two groups, in the fixed geographic reference frame. The error in the filtering effect correction required to produce these opposing 500-m shifts in LF–HF is large, because the two groups are propagating in nearly opposite directions; roughly speaking, because $\sin(30°/2) = 0.26$, the required error is ∼2 km (more quantitatively, considering the individual migration directions, Figure D1b shows that it is ∼2.5 km (red dot in Figure D1b), corresponding to about 0.05 s in each of the Δt_{12} and Δt_{13} time offsets). Because the maximum error in the filtering effect correction due to random cross-correlation errors is only 1/3 of the value used in Figure D1b, random measurement errors could shift the LF–HF separation for the two groups only from −500 m to ∼−330 m. To reduce the LF–HF offset for these two groups to zero would require a systematic error that makes the true filtering effect correction roughly 40% larger than its adopted value, averaged over the region of interest.

In contrast, because the migrations in Figure 8b propagate mostly to the SE (rose diagram in Figure D2a), an error in the filtering effect correction in this direction translates into an almost equal shift in the LF–HF offset. Moving the filtering effect correction by ∼2.5 km to the NNW (red dot in Figure D1b), to make the LF–HF offset be zero for both opposing groups in Figure 8a, would make the LF–HF offset for the other migrations in Figure 8b close to 2.1 km (LF leading HF). The simplest a priori expectation is that all the groups should have roughly similar LF–HF offsets in the reference frame of the migrating front, independent of the migration direction. We therefore search for filtering effect corrections that would minimize the difference between the average LF–HF offset for the E-propagating group (Figure 8a top; 634 LF detections), WSW-propagating group (Figure 8a bottom; 1,265 LF detections) and the other migrations (Figure 8b; 1,580 LF detections) while remaining close to the original measured correction (gray bar in Figure D1b).

We first identify the filtering effect corrections that would make the three mean LF–HF offsets roughly consistent, by allowing the maximum difference in LF–HF offset between the three groups (in practice we compute the maximum difference between the three values) to be up to 400 m. There are 6 qualified corrections in Figure D1b; all distribute roughly along the orientation of the measured filtering effect correction, as required to maintain similar LF–HF offsets, in the reference frame of the migrating front, for the E-propagating and WSW-propagating groups. Among them, the correction leading to the smallest difference between the three mean LF–HF offsets is shown by the open triangle, which produces LF–HF offsets within ±85 m of −865 m. However, the implied error in our filtering effect correction in this case is ∼2.2 km, which seems large. In contrast, the open circle implies an error of only 1.3 km, and leads to the three mean LF–HF offsets being within ±160 m of −570 m (it moves the average LF–HF offsets for the E-propagating group, the WSW-propagating group, and the other migrations to about −730 m, −650 m, and −410 m, from our originally-measured filtering effect corrections of −350 m, −570 m, and +390 m, respectively). This means that the average LF–HF offsets for all three migration groups in this study could be made consistent with one another, at a value of ∼−600 m, for a systematic error in the filtering effect corrections that is only slightly larger than our upper bound for the random cross-correlation errors, or equivalently the spread of the filtering effect corrections in that direction in Figure D1a (±1.1 km).

Data Availability Statement

The seismic data at the permanent stations used in this study came from the Canadian National Seismograph Network (https://www.earthquakescanada.nrcan.gc.ca/stndon/index-en.php). The POLARIS stations are currently offline, but can be accessed through the AutoDRM service (http://www.earthquakescanada.nrcan.gc.ca/stndon/AutoDRM/index-en.php). Figure 2 was produced using the Generic Mapping Tools (GMT) v4.5.18 (https://www.generic-mapping-tools.org/download/). The merged tremor catalogs, developed computer codes for analyses, and all figures of this paper could be found at the archival repository, figshare (https://doi.org/10.6084/m9.figshare.14751069.v1).

Acknowledgments
This work was supported by NSF award EAR-1645145. We would like to thank Michael G. Bostock for the updated LFE catalog in Cascadia and John G. Armbruster for the use of his modified Hypoinverse package. We also would like to thank the two reviewers, Ken Creager and Akiko Takeo, and the Editor, Rachel Abercrombie, for their constructive reviews of this paper.

References

Andrews, D. (1976). Rupture velocity of plane strain shear cracks. *Journal of Geophysical Research*, *81*(32), 5679–5687. https://doi.org/10.1029/jb081i032p05679
Armbruster, J. G., & Kim, W.-Y. (2010). Coherent tremor in the cascadia subduction zone. In *Agu fall meeting abstracts*.
Armbruster, J. G., Kim, W.-Y., & Rubin, A. M. (2014). Accurate tremor locations from coherent s and p waves. *Journal of Geophysical Research: Solid Earth*, *119*(6), 5000–5013. https://doi.org/10.1002/2014jb011133
Barenblatt, G. I. (1962). The mathematical theory of equilibrium cracks in brittle fracture. *Advances in Applied Mechanics*, *7*(1), 55–129. https://doi.org/10.1016/s0065-2156(08)70121-2
Bartlow, N. M., Miyazaki, S., Bradley, A. M., & Segall, P. (2011). Space-time correlation of slip and tremor during the 2009 cascadia slow slip event. *Geophysical Research Letters*, *38*(18). https://doi.org/10.1029/2011gl048714
Bendat, J. S., & Piersol, A. G. (2011). *Random data: analysis and measurement procedures* (Vol. 729). John Wiley & Sons.
Benesty, J., Chen, J., Huang, Y., & Cohen, I. (2009). Pearson correlation coefficient. In *Noise reduction in speech processing* (pp. 1–4). Springer. https://doi.org/10.1007/978-3-642-00296-0_5
Beroza, G. C., & Ide, S. (2011). Slow earthquakes and nonvolcanic tremor. *Annual Review of Earth and Planetary Sciences*, *39*, 271–296. https://doi.org/10.1146/annurev-earth-040809-152531
Bird, P. (2003). An updated digital model of plate boundaries. *Geochemistry, Geophysics, Geosystems*, *4*(3). https://doi.org/10.1029/2001gc000252
Bostock, M. G., & Christensen, N. I. (2012). Split from slip and schist: Crustal anisotropy beneath northern cascadia from non-volcanic tremor. *Journal of Geophysical Research: Solid Earth*, *117*(B8). https://doi.org/10.1029/2011jb009095
Bostock, M. G., Royer, A. A., Hearn, E. H., & Peacock, S. M. (2012). Low frequency earthquakes below southern vancouver island. *Geochemistry, Geophysics, Geosystems*, *13*(11), 12. https://doi.org/10.1029/2012gc004391
Bostock, M. G., Thomas, A. M., Savard, G., Chuang, L., & Rubin, A. M. (2015). Magnitudes and moment-duration scaling of low-frequency earthquakes beneath southern vancouver island. *Journal of Geophysical Research: Solid Earth*, *120*(9), 6329–6350. https://doi.org/10.1002/2015jb012195
Brown, J. R., Beroza, G. C., Ide, S., Ohta, K., Shelly, D. R., Schwartz, S. Y., et al. (2009). Deep low-frequency earthquakes in tremor localize to the plate interface in multiple subduction zones. *Geophysical Research Letters*, *36*(19), 5. https://doi.org/10.1029/2009gl040027
Brown, J. R., Beroza, G. C., & Shelly, D. R. (2008). An autocorrelation method to detect low frequency earthquakes within tremor. *Geophysical Research Letters*, *35*(16). https://doi.org/10.1029/2008gl034560
Chestler, S. R., & Creager, K. C. (2017). Evidence for a scale-limited low-frequency earthquake source process. *Journal of Geophysical Research: Solid Earth*, *122*(4), 3099–3114. https://doi.org/10.1002/2016jb013717
Crosson, R. S. (1976). Crustal structure modeling of earthquake data: 2. Velocity structure of the puget sound region, washington. *Journal of Geophysical Research*, *81*(17), 3047–3054. https://doi.org/10.1029/jb081i017p03047
Farge, G., Shapiro, N. M., & Frank, W. B. (2020). Moment-duration scaling of low-frequency earthquakes in guerrero, mexico. *Journal of Geophysical Research: Solid Earth*, *125*(8), e2019JB019099. https://doi.org/10.1029/2019jb019099
Frank, W. B., Rousset, B., Lasserre, C., & Campillo, M. (2018). Revealing the cluster of slow transients behind a large slow slip event. *Science advances*, *4*(5), eaat0661. https://doi.org/10.1126/sciadv.aat0661
Frank, W. B., Shapiro, N. M., Husker, A. L., Kostoglodov, V., Romanenko, A., & Campillo, M. (2014). Using systematically characterized low-frequency earthquakes as a fault probe in guerrero, mexico. *Journal of Geophysical Research: Solid Earth*, *119*(10), 7686–7700. https://doi.org/10.1002/2014jb011457
Ghosh, A., Huesca-Pérez, E., Brodsky, E., & Ito, Y. (2015). Very low frequency earthquakes in cascadia migrate with tremor. *Geophysical Research Letters*, *42*(9), 3228–3232. https://doi.org/10.1002/2015gl063286
Ghosh, A., Vidale, J. E., Sweet, J. R., Creager, K. C., & Wech, A. G. (2009). Tremor patches in cascadia revealed by seismic array analysis. *Geophysical Research Letters*, *36*(17). https://doi.org/10.1029/2009gl039080
Ghosh, A., Vidale, J. E., Sweet, J. R., Creager, K. C., Wech, A. G., Houston, H., et al. (2010). Rapid, continuous streaking of tremor in cascadia. *Geochemistry, Geophysics, Geosystems*, *11*(12). https://doi.org/10.1029/2010gc003305
Gomberg, J., Agnew, D., & Schwartz, S. (2016). Alternative source models of very low frequency events. *Journal of Geophysical Research: Solid Earth*, *121*(9), 6722–6740. https://doi.org/10.1002/2016jb013001
Gomberg, J., Creager, K. C., Sweet, J. R., Vidale, J. E., Ghosh, A., & Hotovec, A. (2012). Earthquake spectra and near-source attenuation in the cascadia subduction zone. *Journal of Geophysical Research*, *117*(B5). https://doi.org/10.1029/2011jb009055
Hawthorne, J., & Bartlow, N. (2018). Observing and modeling the spectrum of a slow slip event. *Journal of Geophysical Research: Solid Earth*, *123*(5), 4243–4265. https://doi.org/10.1029/2017jb015124
Heaton, T. H. (1990). Evidence for and implications of self-healing pulses of slip in earthquake rupture. *Physics of the Earth and Planetary Interiors*, *64*(1), 1–20. https://doi.org/10.1016/0031-9201(90)90002-f
Holland, P. W., & Welsch, R. E. (1977). Robust regression using iteratively reweighted least-squares. *Communications in Statistics - Theory and Methods*, *6*(9), 813–827. https://doi.org/10.1080/03610927708827533
Houston, H., Delbridge, B. G., Wech, A. G., & Creager, K. C. (2011). Rapid tremor reversals in cascadia generated by a weakened plate interface. *Nature Geoscience*, *4*(6), 404–409. https://doi.org/10.1038/ngeo1157
Hutchison, A. A., & Ghosh, A. (2016). Very low frequency earthquakes spatiotemporally asynchronous with strong tremor during the 2014 episodic tremor and slip event in cascadia. *Geophysical Research Letters*, *43*(13), 6876–6882. https://doi.org/10.1002/2016gl069750
Ide, S. (2008). A brownian walk model for slow earthquakes. *Geophysical Research Letters*, *35*(17). https://doi.org/10.1029/2008gl034821
Ide, S. (2010). Quantifying the time function of nonvolcanic tremor based on a stochastic model. *Journal of Geophysical Research: Solid Earth*, *115*(B8). https://doi.org/10.1029/2009jb000829
Ide, S. (2019). Detection of low-frequency earthquakes in broadband random time sequences: Are they independent events? *Journal of Geophysical Research: Solid Earth*, *124*(8), 8611–8625. https://doi.org/10.1029/2019jb017643
Ide, S., Beroza, G. C., Shelly, D. R., & Uchide, T. (2007). A scaling law for slow earthquakes. *Nature*, *447*(7140), 76–79. https://doi.org/10.1038/nature05780
Ide, S., Shelly, D. R., & Beroza, G. C. (2007). Mechanism of deep low frequency earthquakes: Further evidence that deep non-volcanic tremor is generated by shear slip on the plate interface. *Geophysical Research Letters*, *34*(3). https://doi.org/10.1029/2006gl028890
Ito, Y., & Obara, K. (2006). Dynamic deformation of the accretionary prism excites very low frequency earthquakes. *Geophysical Research Letters*, *33*(2). https://doi.org/10.1029/2005gl025270

Ito, Y., Obara, K., Shiomi, K., Sekine, S., & Hirose, H. (2007). Slow earthquakes coincident with episodic tremors and slow slip events. *Science*, *315*(5811), 503–506. https://doi.org/10.1126/science.1134454

Kaneko, L., Ide, S., & Nakano, M. (2018). Slow earthquakes in the microseism frequency band (0.1–1.0 hz) off kii peninsula, Japan. *Geophysical Research Letters*, *45*(6), 2618–2624. https://doi.org/10.1002/2017gl076773

Kao, H., Shan, S.-J., Dragert, H., & Rogers, G. (2009). Northern cascadia episodic tremor and slip: A decade of tremor observations from 1997 to 2007. *Journal of Geophysical Research: Solid Earth*, *114*(B11). https://doi.org/10.1029/2008jb006046

Katsumata, A., & Kamaya, N. (2003). Low-frequency continuous tremor around the moho discontinuity away from volcanoes in the southwest Japan. *Geophysical Research Letters*, *30*(1), 20-1–20-4. https://doi.org/10.1029/2002gl015981

Klein, F. (2002). *User's guide to hypoinverse-2000, a fortran program to solve for earthquake locations and magnitudes 4/2002 Version* (Vol. 1, pp. 123). USGS. Open File Report 02-171 Version.

La Rocca, M., Creager, K. C., Galluzzo, D., Malone, S., Vidale, J. E., Sweet, J. R., et al. (2009). Cascadia tremor located near plate interface constrained by S minus P wave times. *Science*, *323*(5914), 620–623. https://doi.org/10.1126/science.1167112

La Rocca, M., Galluzzo, D., Malone, S., McCausland, W., & Del Pezzo, E. (2010). Array analysis and precise source location of deep tremor in cascadia. *Journal of Geophysical Research: Solid Earth*, *115*(B6), 68. https://doi.org/10.1029/2008jb006041

Madariaga, R. (1976). Dynamics of an expanding circular fault. *Bulletin of the Seismological Society of America*, *66*(3), 639–666. https://doi.org/10.1785/bssa0660030639

Masuda, K., Ide, S., Ohta, K., & Matsuzawa, T. (2020). Bridging the gap between low-frequency and very-low-frequency earthquakes. *Earth Planets and Space*, *72*, 1–9. https://doi.org/10.1186/s40623-020-01172-8

McCrory, P. A., Blair, J. L., Waldhauser, F., & Oppenheimer, D. H. (2012). Juan de fuca slab geometry and its relation to wadati-benioff zone seismicity. *Journal of Geophysical Research: Solid Earth*, *117*(B9). https://doi.org/10.1029/2012jb009407

Nowack, R. L., & Bostock, M. G. (2013). Scattered waves from low-frequency earthquakes and plate boundary structure in northern cascadia. *Geophysical Research Letters*, *40*(16), 4238–4243. https://doi.org/10.1002/grl.50826

Obara, K. (2002). Nonvolcanic deep tremor associated with subduction in southwest Japan. *Science*, *296*(5573), 1679–1681. https://doi.org/10.1126/science.1070378

Obara, K. (2010). Phenomenology of deep slow earthquake family in southwest Japan: Spatiotemporal characteristics and segmentation. *Journal of Geophysical Research: Solid Earth*, *115*(B8). https://doi.org/10.1029/2008jb006048

Obara, K., & Ito, Y. (2005). Very low frequency earthquakes excited by the 2004 off the kii peninsula earthquakes: A dynamic deformation process in the large accretionary prism. *Earth Planets and Space*, *57*(4), 321–326. https://doi.org/10.1186/bf03352570

Obara, K., Matsuzawa, T., Tanaka, S., & Maeda, T. (2012). Depth-dependent mode of tremor migration beneath kii peninsula, nankai subduction zone. *Geophysical Research Letters*, *39*(10). https://doi.org/10.1029/2012gl051420

Peng, Y., & Rubin, A. M. (2017). Intermittent tremor migrations beneath guerrero, mexico, and implications for fault healing within the slow slip zone. *Geophysical Research Letters*, *44*(2), 760–770. https://doi.org/10.1002/2016gl071614

Peng, Y., Rubin, A. M., Bostock, M. G., & Armbruster, J. G. (2015). High-resolution imaging of rapid tremor migrations beneath southern vancouver island using cross-station cross correlations. *Journal of Geophysical Research: Solid Earth*, *120*(6), 4317–4332. https://doi.org/10.1002/2015jb011892

Press, W. H., Teukolsky, S. A., Vetterling, W. T., & Flannery, B. P. (2007). *Numerical recipesThe art of scientific computing* (3rd ed.). Cambridge university press.

Rousset, B., Bürgmann, R., & Campillo, M. (2019). Slow slip events in the roots of the san andreas fault. *Science advances*, *5*(2), eaav3274. https://doi.org/10.1126/sciadv.aav3274

Rubin, A. M., & Armbruster, J. G. (2013). Imaging slow slip fronts in cascadia with high precision cross-station tremor locations. *Geochemistry, Geophysics, Geosystems*, *14*(12), 5371–5392. https://doi.org/10.1002/2013gc005031

Shelly, D. R. (2010). Migrating tremors illuminate complex deformation beneath the seismogenic san andreas fault. *Nature*, *463*(7281), 648–652. https://doi.org/10.1038/nature08755

Shelly, D. R., Beroza, G. C., & Ide, S. (2007a). Complex evolution of transient slip derived from precise tremor locations in western shikoku, Japan. *Geochemistry, Geophysics, Geosystems*, *8*(10), 68. https://doi.org/10.1029/2007gc001640

Shelly, D. R., Beroza, G. C., & Ide, S. (2007b). Non-volcanic tremor and low-frequency earthquake swarms. *Nature*, *446*(7133), 305–307. https://doi.org/10.1038/nature05666

Shelly, D. R., Beroza, G. C., Ide, S., & Nakamula, S. (2006). Low-frequency earthquakes in shikoku, Japan, and their relationship to episodic tremor and slip. *Nature*, *442*(7099), 188–191. https://doi.org/10.1038/nature04931

Thomas, A. M., Beroza, G. C., & Shelly, D. R. (2016). Constraints on the source parameters of low-frequency earthquakes on the san andreas fault. *Geophysical Research Letters*, *43*(4), 1464–1471. https://doi.org/10.1002/2015gl067173

Wech, A. G., & Creager, K. C. (2007). Cascadia tremor polarization evidence for plate interface slip. *Geophysical Research Letters*, *34*(22). https://doi.org/10.1029/2007gl031167

Wech, A. G., & Creager, K. C. (2008). Automated detection and location of cascadia tremor. *Geophysical Research Letters*, *35*(20). https://doi.org/10.1029/2008gl035458

Wu, C., Guyer, R., Shelly, D., Trugman, D., Frank, W., Gomberg, J., et al. (2015). Spatial-temporal variation of low-frequency earthquake bursts near parkfield, california. *Geophysical Journal International*, *202*(2), 914–919. https://doi.org/10.1093/gji/ggv194